A New Experiment for the HERA Collider
Expression of Interest

Author list under construction

April 16, 2003

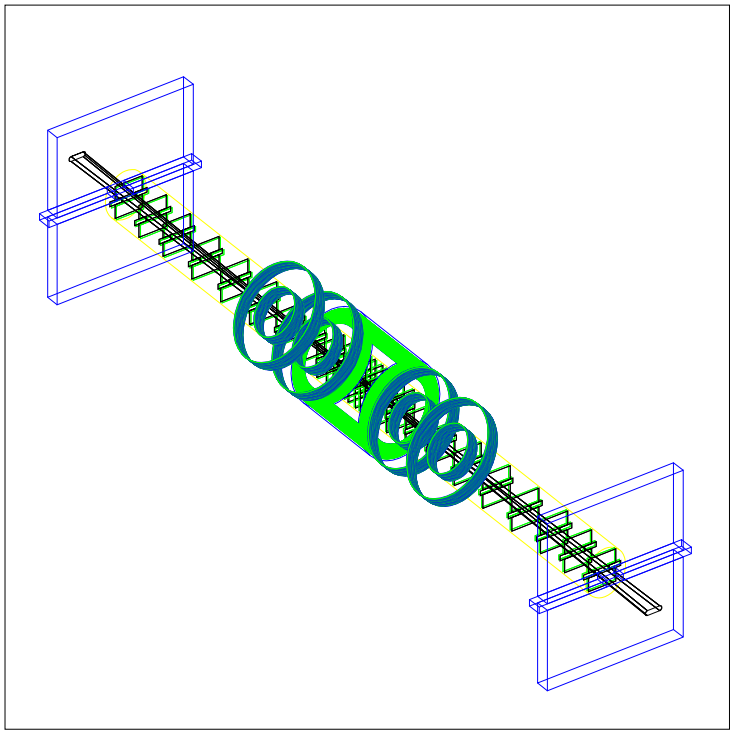

1 Introduction

Quantum Chromodynamics is now widely acknowledged to be the correct theory for the strong hadronic interactions. Knowing the correct Lagrangian for the theory does not however imply that we know everything we want to know about the strong interactions. Experimental observations such as the confinement of color or the energy dependence of scattering cross sections cannot today be predicted from the QCD Lagrangian. These are striking results which should be calculable from first principles if we are to claim to understand our universe.

We describe with this document a program dedicated to the study of the strong hadronic interactions with a unique probe - the HERA accelerator. The immediate aim is to push our understanding of these interactions to a new level. A possible outcome is a completely new way of thinking about the fundamental constituents and their interactions.

One might ask, "How is it possible that experiments on nucleon structure in the energy range of HERA will advance our understanding of elementary particles and forces when the Standard Model already predicts everything ?" In this document, we describe the particulars of measurements which have not yet been performed, or which have not been performed with enough accuracy. To place these in context, we recall a few historical events reflecting times when experiments were done in regions where "everything is understood."

1. In the early twentieth century, the force (electromagnetism) and components involved in atoms were basically known after the discovery of the electron and the Rutherford experiment. And yet knowing the force and the constituents was not the entire story: important input from experiments on atoms were essential to finally understanding Quantum Mechanics. Today, even if QCD, quarks, and gluons were all true as we now understand them, there could be much more when the full story is completed.

2. In the 1960's, verified predictions made it clear that SU(3) and the quark model explained hadronic spectra as then understood. At the same time, even some originators of these ideas doubted whether quarks had any physical reality. The first deep inelastic experiments, which many thought would be unproductive, unexpectedly demonstrated the physical reality of the quarks and provided a crucial step to realizing QCD as the theory of the strong force and one backbone of the Standard Model. Since then, experiments have continued to verify the nature of QCD for high momentum transfers, where theory predicts much more than experiments can measure. At the same time, experiment leads theory in delineating hadronic structure and the behavior of strong interactions at energies corresponding to the bound states found in the everyday world.

HERA is particularly well suited to study radiation patterns in strong interactions, and all the measurements described in this document have as basic goal the understanding of these radiation patterns. The structure function measurements will probe the evolution of the parton densities as longitudinal and transverse distance scales are varied, while the forward jet measurements will allow detailed and direct tests of our understanding of radiation over a large and fixed rapidity interval. Measurements of exclusive processes will allow for a much more detailed mapping of the distribution of strongly interacting matter in hadrons, while measurements of particle production and correlations will yield sensitive tests of perturbative and non-perturbative QCD calculations. These measurements will be performed in much wider kinematical regions than possible with ZEUS and H1, thus providing greatly enhanced sensitivity to the underlying physics. Heavier targets than the proton will allow the study of nuclear matter in a more uniform medium, and may in many ways be simpler to understand theoretically. HERA with heavy nuclei (e.g., Mercury) will allow to study a novel state of matter - the saturated gluon state or Color Glass Condensate. Revealing experimentally the CGC would be pivotal in understanding the high energy limit of QCD and the origin of quark and gluon distributions.

We first review the physics topics which we consider to be the highlights of the proposed program. The increased sensitivity to the correct understanding of radiation in strong interactions is made clear in these sections. We then describe some first ideas on what the optimized detector for this physics would look like. We note that the physics described in the following sections cannot be carried out with HERA-II. This second phase of HERA running is focused on high Q^2 physics, which requires high luminosities. These are achieved by placing combined dipole/quadrupole magnets very near the H1 and ZEUS interaction points, thus limiting

access to the small-x, low Q^2 physics which would be a central element in the proposed program. Also, many of the topics one would like to study require a different type of detector than the current H1 and ZEUS detectors.

We close with a brief discussion of a possible time scale for the construction of a new detector and what we would consider to be a viable running plan.

2 Physics program highlights

2.1 Precision structure function measurements

2.1.1 Motivation

To date, the most striking results uncovered by the HERA collider experiments pertain to the regime of low Bjorken x values. They can be summarized as follows:

1. The F_2 structure function was found to rise steeply with decreasing x and increasing Q^2, in sharp contrast to the photoproduction cross section which was found to follow a mild increase with W, as observed in hadron-hadron scattering.

2. A substantial percentage of deep-inelastic scattering (DIS) events (about 10%) was found to be characterized by the presence of a large rapidity gap in the final state, located in the proton direction.

3. The cross section for exclusive J/ψ photo-production was found to increase steeply with increasing W, in contrast to the cross section for light vector meson photo-production, which exhibits a slow W dependence. At high Q^2 also the cross section for exclusive light vector meson production was found to acquire a steeper W dependence.

4. The cross section for exclusive DIS production of a real photon was found to substantially exceed the expectations for the Bethe-Heitler process, and the excess is understood as originating from deeply virtual Compton scattering (DVCS) off partons in the proton.

5. The cross section for forward jet or π^0 production with large transverse momentum exceeds the expectations based on DGLAP type of radiation patterns. The same is true for DIS production of jets with transverse energy squared greater than the Q^2 of the interaction.

Each of the observed phenomena has a natural explanation within perturbative QCD (pQCD), even though quantitative calculations may not be in perfect agreement with experimental measurements.

1. The rise of F_2 with decreasing x and increasing Q^2 is well described by standard DGLAP evolution in NLO. In fact the solution of the DGLAP evolution equations holds down to Q^2 values as low as 1 GeV^2.

2. The large rapidity gap events are attributed to diffractive scattering of the virtual photon off the (soft) Pomeron, emitted by the unscathed proton. The analysis of the partonic content of the Pomeron points to a large gluonic contribution to the Pomeron structure.

3. Within pQCD the fast increase of F_2 with decreasing x is due to a fast increase of the gluon density in the low x region due to radiation processes. In the presence of a large gluon density, coherent effects are expected. The exclusive vector meson production and DVCS is understood as due to the exchange of a two-gluon ladder.

4. The excess of forward jets and of jets with transverse energy squared larger than Q^2 can be accommodated by introducing the concept of the hadronic structure of a virtual photon, by analogy to the hadronic structure of the real photon.

While each of the explanations may be satisfactory, they entail problems which prevent a consistent understanding of low x physics within QCD. Here is a brief summary of the problems.

1. The success of the NLO DGLAP equations in describing the evolution of F_2 over four-orders of magnitude in x and in Q^2 may be a proof of the validity of this approach. However, the global fits involve anywhere between 18 to 30 parameters, and there is no mathematical proof of the uniqueness of the solution. In fact, in order to accommodate the relatively low Q^2 and low x region of the F_2 measurements one has to resort to negative gluon densities. While for some this is still acceptable, as gluons are not

physical observables (an argument disputed by others), it is clear that a negative value of the longitudinal structure function signals the breakdown of the mathematical formalism. Moreover, there are theoretical arguments for the presence of large higher twist contributions to the longitudinal (F_L) and transverse (F_T) structure functions which cancel in the calculation of F_2. If true, this would invalidate the DGLAP approach, in spite of its numerical success.

2. The DGLAP type of radiation can produce large rapidity gaps (LRG) which are exponentially suppressed. This cannot explain the large fraction of events observed. If, on the other hand the origin of the large rapidity gap is purely soft in nature (Pomeron), it may be included in the initial condition from which the evolution starts. One would then expect that the distribution of the fraction of the proton momentum carried by the Pomeron, $x_{I\!P}$, is universal. The results obtained at HERA indicate that the $x_{I\!P}$ distribution changes with Q^2. While the explanation may lie in that there is more than one soft mechanism contributing to LRG production, each with different $x_{I\!P}$ distribution and parton decomposition, this is certainly not obvious.

3. The exchange of two-gluon ladders is not part of the DGLAP evolution. It constitutes a higher twist contribution to F_2. No attempt was ever made to quantify the fraction of the total DIS cross section leading to exclusive final states. Rough estimates point to a contribution which could be as high as a few percent.

4. The need to introduce the hadronic structure of the virtual photon to describe final states with large transverse energy jets points to a pattern of radiation different from that of the DGLAP evolution, in which the transverse momenta of radiated partons are ordered in transverse mometum k_T and the one struck by the virtual photon has the largest k_T (subject to fluctuations due to final state radiation). The events which cannot be accommodated by the DGLAP evolution constitute about 5% of the total cross section. They could very well be representative either of higher order corrections or of patterns expected in the BFKL regime where there is no ordering in k_T.

All of the above may indicate that in fact there are deviations from the DGLAP evolution. This in itself represents a very interesting QCD phenomenon, but it also puts in doubt the reliability of parton distributions derived from the measurements of F_2, with consequences for our ability to predict what will happen in an enlarged phase space, as expected at future colliders.

2.1.2 Proposed measurements

The measurements of the F_2, F_L and xF_3 structure functions of the nucleon were instrumental in discovering the point-like nature of hadron constituents, quarks and gluons, in establishing QCD as the theory of strong interactions and in determining the value of the strong coupling constant. Today, the measurements of F_2 cover a large phase space in Bjorken x and Q^2, as shown in Fig. 1, and are used to determine a universal set of parton densities to be used for predicting and calculating processes in phase space regions within and beyond the probed space. The conventional approach is to postulate the x dependence of parton densities at some fixed Q_0^2 and to fit the shape parameters, so that the parton densities evolved through the DGLAP evolution equations reproduce best the F_2 data. There are many unknowns in this procedure. In particular

- the shape and flavor of the parton densities cannot be derived from first principles,
- the scale at which the perturbative evolution can be safely applied is not known,
- there is no prior knowledge when to stop the perturbative expansion of the splitting functions and the corresponding coefficient functions entering the DGLAP formalism.

Using the NLO DGLAP evolution equations, the shape parameters can be very well fitted to the F_2 data, down to Q^2 values as low as $1\,\mathrm{GeV}^2$ [1, 2, 3]. However, at low Q^2 values, the solution [1, 2] requires a negative gluon density at low x. While it may be disputed whether unobservable gluon densities can be negative, F_L,

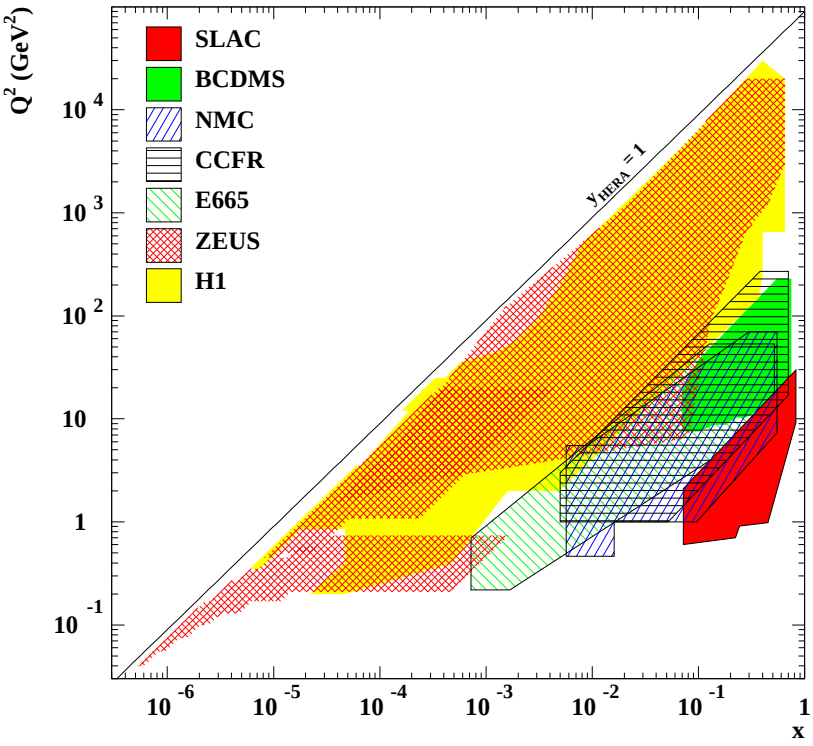

Figure 1: x and Q^2 plane covered by measurements of F_2 in charged lepton-nucleon scattering.

as a physical observable, has to be positive. For DGLAP fits which include measurements of high transverse momentum jets at the Tevatron [4, 5], and therefore require larger gluon content at high x, negative F_L values for $x < 2 \cdot 10^{-4}$ appear already at $Q^2 = 2\,\mathrm{GeV}^2$. This puts in doubt the validity of the DGLAP formalism in this low x and low Q^2 region. Moreover, it becomes apparent that a good fit to the F_2 data does not guarantee the applicability of the DGLAP evolution equations, at least in NLO. This is especially true in the low x region, where the lever arm in Q^2 is small.

One striking experimental result from the first run of HERA is the observation of a transition in the behavior of F_2 at $Q^2 \approx 0.5$ GeV^2. Below this virtuality, the virtual photon-proton cross section has a very similar energy dependence to that seen in hadron-hadron scattering. Above this Q^2, the cross sections show a steeper energy dependence (see Fig. 2). The location of this transition is particularly interesting, as it is near the perturbative regime, and far from the scale set by the dimensions of the proton. The quality of the existing data in the transition region is not as high as in other regions, because this corresponds to a geometrical location for the scattered electron where the H1 and ZEUS detectors have very limited acceptance. A detector dedicated to this region could make precision measurements exactly in the range where the data indicates something interesting is taking place. The transition in the behavior of the energy dependence indicates a transition from partonic degrees of freedom to hadronic degrees of freedom (formation of constituent quarks), which would imply a connection to color confinement.

At the other end of the x scale, $x > 0.5$, higher twist effects are known to play an important role. At $x > 0.6$ higher twist contamination plays a role up to Q^2 of about $100\,\mathrm{GeV}^2$ and is simply parameterized in the fit procedure. Via sum rules, the large x region is important in the momentum balance of the parton densities, which then affects the densities at low x. This interplay affects the determination of α_S from the evolution of F_2. The region of large x is important in the calculation of moments of parton distributions which can be directly compared to lattice calculations.

Importance of F_L At low x and relatively low Q^2, there are various dynamical arguments why the NLO DGLAP conventional approach may fail. At low x, higher order perturbative corrections may become im-

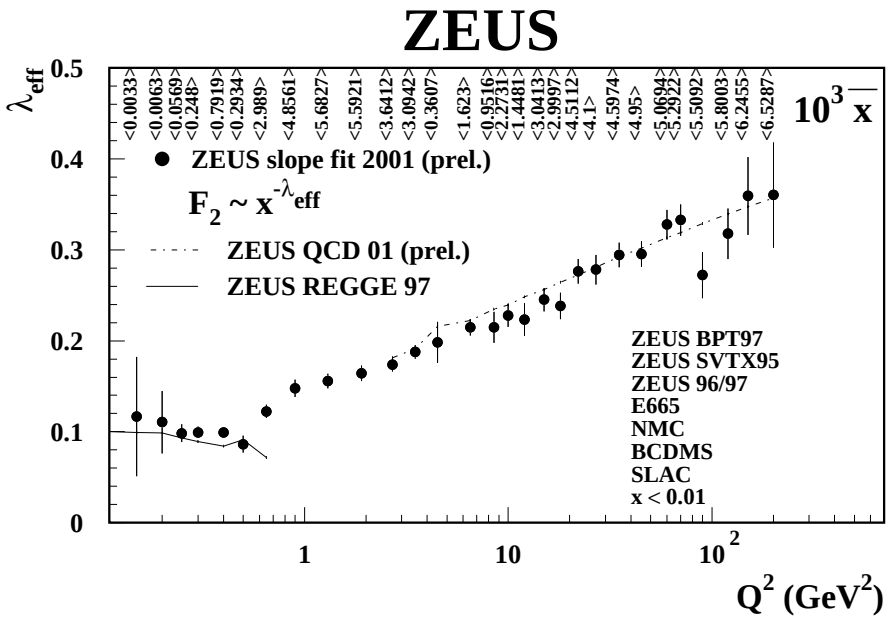

Figure 2: The logarithmic derivative of $\partial F_2/\partial \ln x$, λ_{eff}, as a function of Q^2. Also shown are the values of x, averaged over the range in which λ_{eff} is determined.

portant and possibly the fixed-order perturbative expansion in the strong coupling constant α_S may become inadequate [6, 7]. Present F_2 measurements alone are not sufficient to address these issues. One of the main reasons is that in the F_2 analysis there are only two experimental inputs, $F_2(x, Q^2)$ and $\partial F_2(x, Q^2)/\partial \ln Q^2$. They allow to determine quark and gluon densities, provided the theoretical framework is fixed. The latter can only be checked if other observables are available. Such an observable is the longitudinal structure function.

The effect of using the DGLAP evolution equation at LO, NLO and NNLO for extraction of the gluon density and for the calculation of the corresponding F_L is shown in Fig. 3. The observed effects are quite dramatic especially at low Q^2.

The proper treatment of heavy flavor production in the low x regime is very important [8]. Various schemes have been proposed and their prediction for the charm contribution to F_2, F_2^c, agree to within few percent. However, the variations for the expected F_L^c are very large, as shown in Fig. 4.

In the region where F_2 rises steeply with decreasing x, the parton densities are large and one might expect coherent effects, such as multi-parton interactions, leading to saturation (shadowing) effects in the interaction cross section of the virtual photon with the proton. The observed copious presence of diffractive events in the DIS regime could be one of the manifestations [9]. There are theoretical arguments for the presence of higher twist effects, positive for F_L and negative for F_T ($F_2 = F_L + F_T$), that would approximately cancel for F_2 [10], invalidating however the leading twist DGLAP approach. The dipole model of DIS [11], in which the photon fluctuates into a $q\bar{q}$ pair before interacting with the proton, in a realization proposed by Golec-Biernat and Wuesthoff [12], seems to have all these dynamical properties and will be used as a reference. The comparison between the NLO calculations of F_L and the calculation of F_L in the dipole model is shown in Fig. 5. Also shown are the present measurements of F_L by the H1 experiment [13]. The differences are representative of the contribution of positive higher twists in F_L. The most striking difference is in the Q^2 dependence of F_L at fixed x, where with adequate measurement precision, it should be possible to distinguish even between the NNLO and the dipole model expectations.

F_2 at small and large x One of the important parameters in the study of high energy processes is the logarithmic derivative λ of F_2, defined as

$$\lambda = -\partial F_2/\partial \ln x\,.$$

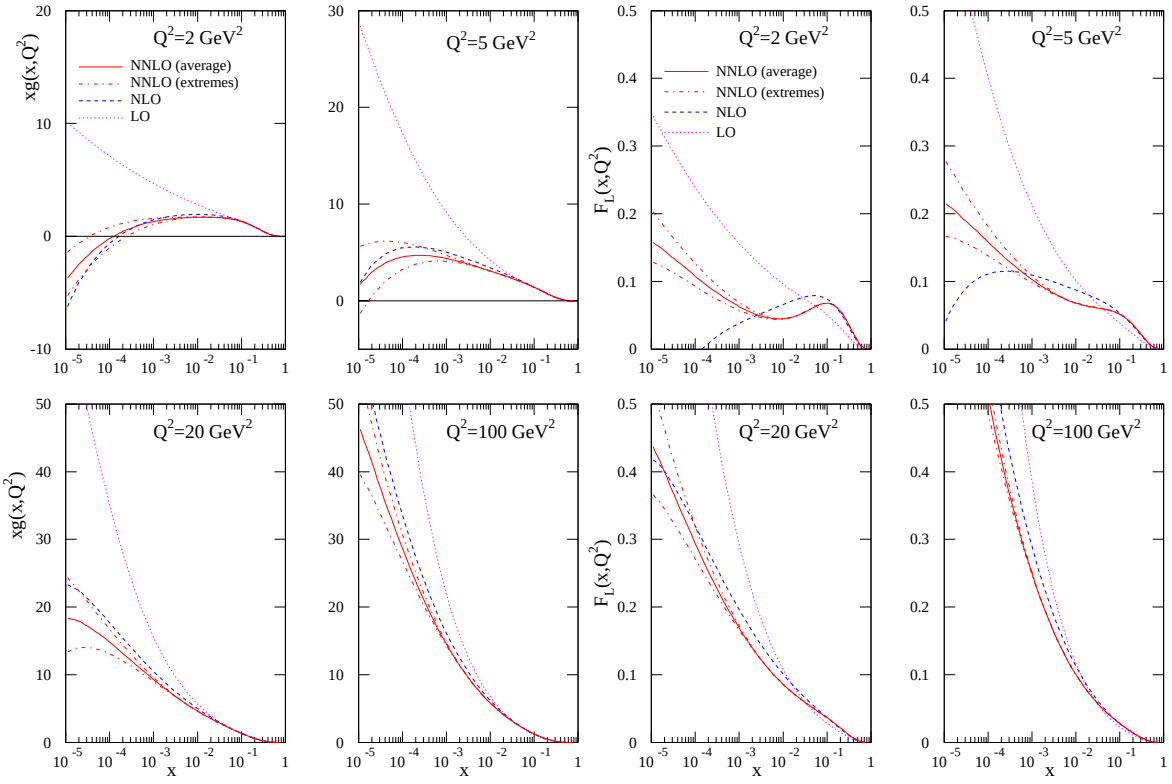

Figure 3: Solution of the DGLAP evolution equation for gluons (left) at different orders of perturbative expansion and the corresponding expectations for F_L (right), as a function of x for fixed Q^2 values.

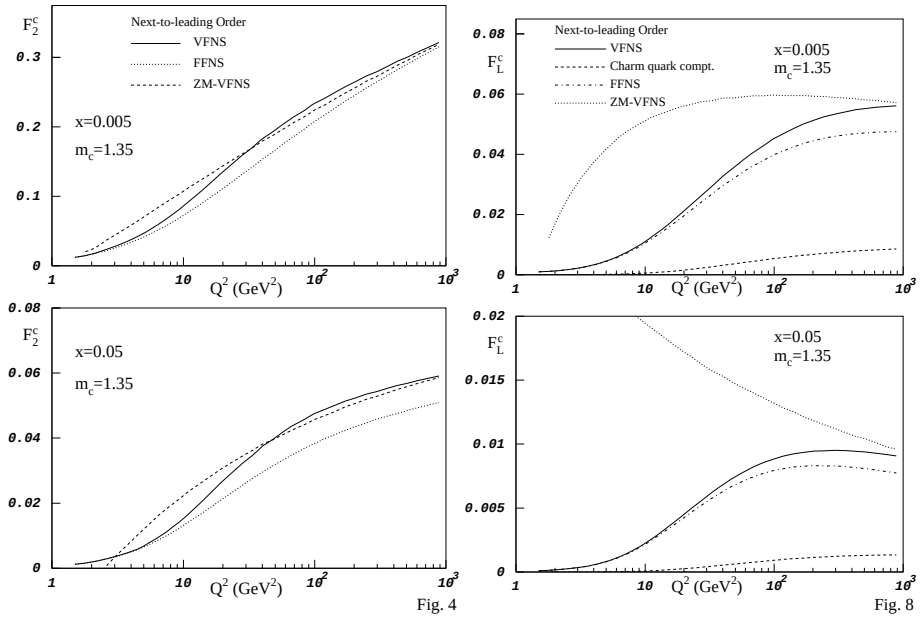

Figure 4: Expectations from DGLAP evolution equations for charm contribution to F_2 (left) and F_L (right) for various heavy-flavor schemes, as denoted in the figure.

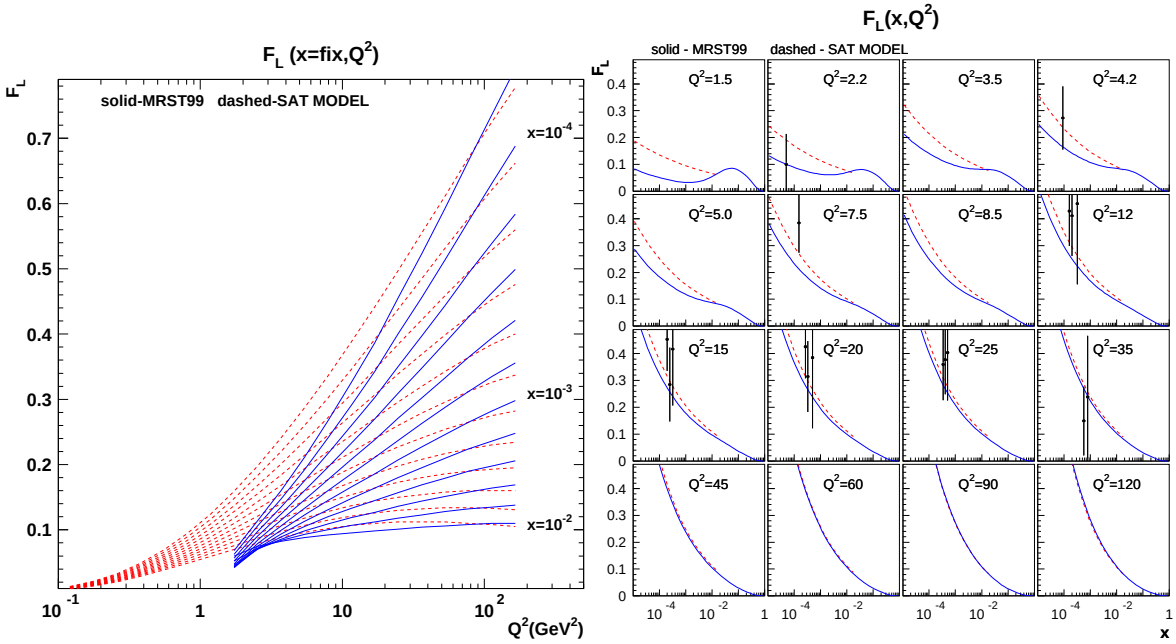

Figure 5: Comparison of the expectations for the Q^2 dependence at fixed x (left) and x dependence at fixed Q^2 (right) of F_L in the DGLAP approach (MRST99) and the saturation dipole model.

Its value is related to the contribution of soft and hard dynamics in the (virtual) photon-proton interactions. The ability to establish a region of dominance of hard physics is crucial in testing the pQCD approach to exclusive processes, the interest of which will be discussed later. The present data seem to point to a sharp transition, which occurs around $Q^2 \approx 0.5\,\mathrm{GeV}^2$ as shown in Fig. 2. It is important to determine the value of λ as a function of Q^2, starting from the baseline at $Q^2 \simeq 0$, in matching intervals of x.

No measurements of F_2 are available for $x > 0.75$ in the large Q^2 region, where higher twist effects are likely to disappear. The non-perturbative corrections to F_2 at large x are expected to scale like $1/Q^2(1-x)$ [14]. If this claim can be verified by performing measurements up to the highest x values, this would give a very important handle on the parton densities at large x. This is important for constraining the momentum balance of the partons and therefore has also implications for the low x region. The current H1 and ZEUS detectors are only able to measure large-x events at very high Q^2, i.e., with small statistics. The main limitation is the acceptance of the detector to very forward jets. A new detector, designed with this physics in mind, would be capable of extending the large-x measurements to much lower Q^2, thus allowing for significant event rates and the ability to extract precision cross sections.

Required precision To validate the universality of parton densities derived from the HERA data, F_L has to be measured in the region of $1 < Q^2 < 20\,\mathrm{GeV}^2$ with a precision of about 5%. This would allow to distinguish between the various theoretical approaches at a 4σ level.

The precision achieved in the measurements of F_2 at HERA has reached about 2%. This leads to an error of λ of about 5% for $\lambda = 0.2$. In the transition region of interest $\lambda \simeq 0.1$, therefore, all efforts should be made to measure F_2 at low Q^2 with a precision better than 2%.

2.2 Exclusive processes

Processes where the target proton is scattered elastically provide an essentially new element of information compared to inclusive reactions. Whereas the Bjorken variable x encodes information on the *longitudinal* momenta of quarks and gluons in a fast moving proton, the square of the four-momentum exchanged at the proton vertex, t, reflects the structure of a hadron as an extended object in the plane *transverse* to its direction of flight. Together with the x dependence this "impact parameter" representation provides a *three dimensional* image of the proton [15, 16, 17]. In particular, the change of the t dependence with x (i.e. diffractive shrinkage) is very different according to whether short- or long-distance dynamics is at play, and has been argued to be deeply connected with the physics of confinement [18].

The formalism of generalized parton distributions (GPDs) [19, 20, 21, 22, 23] provides a solid theoretical framework for describing processes like $\gamma^* p \to \gamma p$ and $\gamma^* p \to \rho p$ at large photon virtuality Q^2. It allows one to specify exactly *how* the proton structure is probed in these processes and makes the Q^2 dependence predictable in a way analogous to the DGLAP evolution of conventional parton densities. Exclusive processes are also well suited to study physics beyond a DGLAP based description, in particular the phenomenon of saturation [24]. Saturation is expected to set in earlier at smaller impact parameters, where partons should be more dense than in an average over the proton size.

2.2.1 Vector meson production

By studying the t dependence of the cross section for elastic vector-meson production one can get access through a Fourier transform to the dipole-proton elementary amplitude with impact parameter dependence and have a unique signature for saturation.

It is expected that the dipole-proton amplitude $N(r,b,x)$, where r is the size of the dipole and b the impact parameter, will have a shape as illustrated in Fig. 6. When $N = 1$ the unitarity limit is reached which is equivalent to the scattering on a black disk. One expects that this will happen first for small values of impact parameter, i.e., for the most central collisions. When the energy is increased, the black regime is going to extend

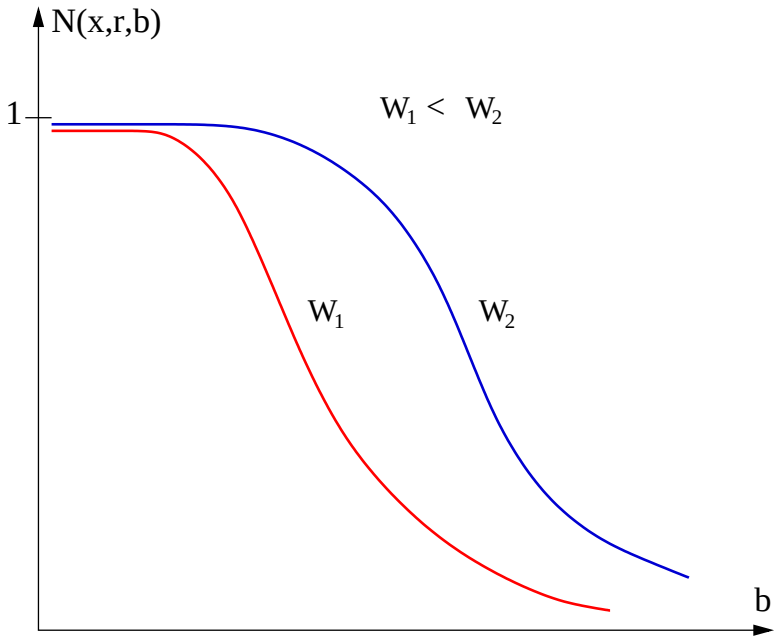

Figure 6: Expectations for the dipole-proton amplitude as a function of impact parameter for different energy regimes.

to higher values of impact parameter, that is to more peripheral collisions. First theoretical studies [24] have shown that to get precise information about the amplitude profile at sufficiently small impact parameters close

to $b \sim 0$, one would need to know the cross section for elastic vector-meson production up to $|t| \simeq 1.5\,\mathrm{GeV}^2$. For fixed $b \simeq 0$, it is expected that when the unitarity limit is reached, then further increases of the energy will result in a constant amplitude. On the other hand, looking at larger values of b, where the amplitude is still far from saturation, one would see the increase of the dipole cross section with increasing energy.

2.2.2 DVCS

Exclusive electroproduction of photons (deeply virtual Compton scattering, DVCS) and of vector mesons are complementary in several respects. DVCS is under better theoretical control since at large Q^2 the structure of both photons is needed at small distance, where it is calculable, whereas a meson wave function represents an additional theoretical unknown. Furthermore, DVCS is closest in its dynamics to inclusive DIS and thus provides a bridge between exclusive and inclusive processes.

The first data on DVCS have already provided a very interesting insight into the possible structure of GPDs [25]. The global QCD analysis of the DVCS cross sections, similar to that of the DGLAP analysis of F_2, requires a larger phase space coverage than presently available, as well as data with improved statistical significance. This cannot be achieved with the HERA-II running where there is no access to low Q^2 events. In order to attempt a three-dimensional mapping of the proton structure one needs to measure the t distribution of the DVCS process, which cannot be performed with the present HERA collider experiments.

2.2.3 Detector requirements

For the exclusive processes to provide information on the scattering amplitude or the GPDs it is essential that the process be elastic. In particular the efficiency to detect events with proton dissociation has to be very high, even for low mass dissociative states. In present analyses, the contribution of proton dissociation contributes the highest systematic error to the measurements of the t distribution.

In case of DVCS, the measurement of t requires a good resolution on the energy of the final state photon and electron, as well as a good angular resolution. Therefore it is mandatory to reconstruct the vertex of the interaction. The resolution on t may be improved by using kinematic constraints. Studies show that assuming a known vertex and the photon energy resolution of $0.14\sqrt{E_\gamma}$, and deriving the scattered electron energy from kinematic constraints, the t distribution of DVCS can be measured up to t of about $1\,\mathrm{GeV}^2$ for an exponential t distribution with a slope of $5\,\mathrm{GeV}^{-2}$. For higher values of the slope the range of t will be appropriately smaller.

One of the important parameters in the study of exclusive processes is the logarithmic derivative $\delta = \partial\sigma_{\gamma^* p}/\partial \ln W$. The value of δ is a measure of the hardness of the process. The error on δ crucially depends on the range of W in which the cross section is measured. In the present analysis of VM production, this range is usually restricted to be between 50 to 120 GeV by the tracking detectors. The error on δ is inversely proportional to the range. If the full range of W accessible at HERA were available for exclusive processes, the error of δ could be decreased by factor 3, for the same integrated luminosity as presently available.

2.3 Forward jets and particle production

2.3.1 Introduction and Motivation

In the following, three poorly understood areas are discussed:

- **parton branching**
  The basic evolution equations for parton branching, the DGLAP and BFKL equations, are expected to be valid in certain regions of phase space only. The CCFM [26, 27, 28, 29] and LDC [30, 31, 32, 33] formalisms combine in a consistent way some features of the DGLAP and BFKL evolution equations and should be superior to both of them when details of the final state are investigated. However, as all of them are approximations to the complete and complicated parton branching process, they naturally are expected to show deficiencies when sufficiently precise tests are performed.

  It has been observed that improving the CCFM/LDC splitting function to include also the DGLAP-like (non-singular) terms results in a worse description of the initial state branching processes. This failure indicates that our understanding and modeling of branching processes is far from satisfactory. It might be that multiple parton exchange mechanisms are at work and have to be included. Already in the BFKL and CCFM/LDC description bare gluons have been replaced by so-called reggeized ones, i.e. gluons which include a cloud of virtual corrections (dressed gluons). This approach, however is just a first step towards the full consideration of multi-parton exchange processes, including the exchange of multiple ladder cascades. In this scenario, a more advanced theoretical method than the conventional parton level perturbative calculation is needed.

- **QCD vacuum**
  The vacuum state in QCD has a highly non-trivial structure and contains both a gluon condensate and a quark (chiral) condensate. Although the magnitude of both condensates can be estimated to a fair degree, the more detailed properties of the vacuum state are still unknown. These properties are responsible for the confinement phenomenon, they determine the non-perturbative hadronization process, and they affect the properties of reactions with vacuum quantum number exchange, i.e. the nature of the Pomeron and soft and hard diffraction.

  In the string hadronization model the *gluon condensate* is treated as a dual super-conductor [34], and particle production is described as a tunneling process in a flux tube or a vortex line. In the "Disoriented Chiral Condensate" the mechanism responsible for particle production is instead related to the *quark condensate* [35, 36]. Perhaps both mechanisms contribute in nature, possibly in different ratios in different reactions. To resolve these questions more detailed data are needed for charge- and $p_\perp$ correlations, K/π ratios, etc.. We also note that some experiments indicate differences between hadronization in e^+e^--annihilation and in DIS or hadronic collisions, as described below.

  If the nucleon is associated with a topological singularity in the pion field, as in the Skyrme model, the vacuum properties should influence not only diffractive scattering, but also peripheral collisions with pion exchange.

- **non-perturbative particle production**
  In collisions between electrons and deuterons a comparison between the proton and neutron properties can be made. The fragmentation region of the proton- or neutron-remnant has never been studied in detail. The primordial k_t-distribution of partons in the nucleon is poorly known, although some measurements indicate the need for relatively large intrinsic k_t. However, these measurements cannot distinguish whether the large k_t needed is intrinsic to the colliding hadron or a result of the parton branching process. whether it was The universality of jet fragmentation is a basic assumption for the hadronization process in most theoretical approaches. However, some experimental analyses indicate that the ratio between strange and non-strange quarks is not the same in e^+e^--annihilation as in DIS or hadronic collisions. It is therefore very interesting to investigate whether there are differences in the hadronization when going from the proton fragmentation region to the central region, which is expected to be very similar to

e^+e^--annihilation. This could be studied by measuring the production of kaons, baryons, and pions as a function of rapidity.

It should be pointed out that the target region has been studied in some detail by the EMC experiment, but there the x values were not small enough (W^2 too small) to properly probe the perturbative QCD branching process. Since QCD processes will create a significant background in the search for signals of new physics it is obvious that a better understanding of the parton branching processes, the QCD vacuum and the universality of fragmentation are necessary.

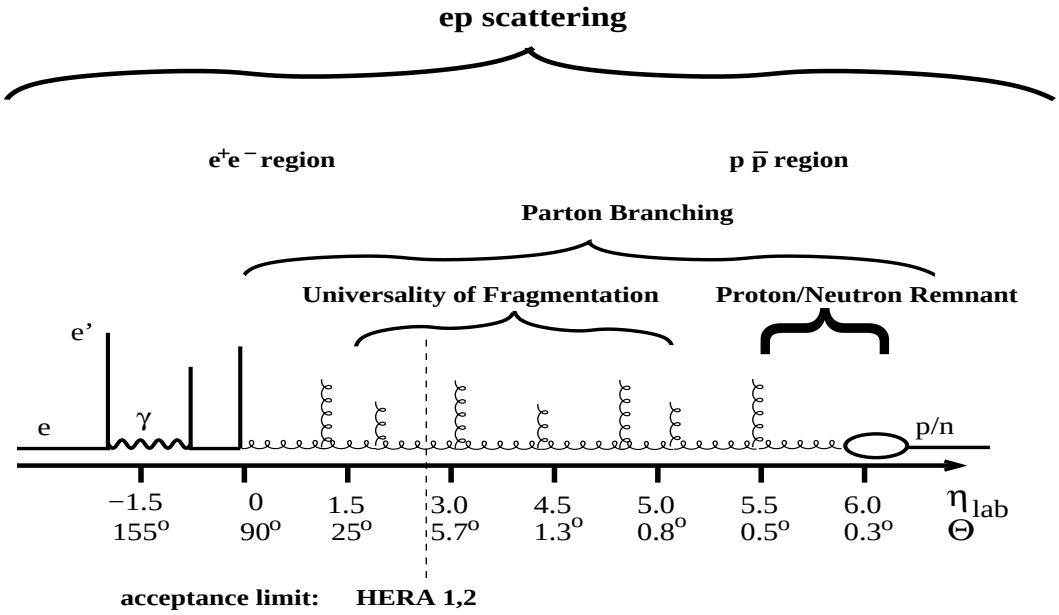

Figure 7: The rapidity range at the HERA laboratory - frame.

2.3.2 The experimental situation

- The hadronic final state in $e^+e^- \to q\bar{q}(+gluons)$ has been precisely measured from low energy experiments up to the highest possible energies measured at LEP. The underlying QCD processes are calculated in perturbation theory up to $O(\alpha_S^2)$. The partonic final state is supplemented with higher order QCD radiation in the form of leading log parton showers and is then fragmented into visible hadrons via non-perturbative hadronization models, like PYTHIA [37] or HERWIG [38]. The hadronization models are tuned finally to describe the final state in e^+e^- reactions.

- The situation in $p\bar{p}$ reactions is completely different. Whereas the underlying hard scattering processes can be calculated in perturbation theory, the description of the hadronic final state is more complicated, as the incoming partons, quarks and gluons, undergo initial state branching processes, which are initiated by partons from the non-perturbative phase of the colliding hadrons.

- The hadronic final state in ep reactions forms a bridge between the well understood situation in e^+e^- and the less-understood situation in $p\bar{p}$. In the rapidity region of the virtual (quasi-real) photon, the hard scattering process is expected to be similar to the e^+e^- case, whereas moving towards the fragmentation region of the proton, we enter a situation similar to $p\bar{p}$. The advantage of ep scattering is the possibility to cover the full range from the photon fragmentation region, which can be described by perturbative QCD, up to the proton fragmentation region, which might be described by collective phenomena only. Multiple scattering processes are essential for a reasonable description of QCD processes in $p\bar{p}$ reactions. However, due to the complicated nature of these processes, it seems to be nearly impossible to study the

effects in detail in $p\bar{p}$. One of the unique advantages of the HERA ep collider is that with decreasing Q^2 multiple interactions become more and more important, until eventually a situation like in $p\bar{p}$ is reached for $Q^2 = 0$. Thus these effects can only be studied at HERA in an experimentally controlled manner.

From the above it is clear that it is necessary to cover as large a rapidity range as possible to measure this highly unexplored and challenging region of QCD. We still lack a proper theoretical framework to describe and study collective phenomena, and it is clear that without experimental investigation we will not have the data to develop such a framework.

The rapidity range covered by HERA is shown in Fig. 7, together with indications where the various effects are expected to show up.

2.3.3 Experimental program

Parton branching - forward jet measurement The cross section for the production of a jet in the proton direction (a forward jet) has been advocated as a particularly sensitive measure of small x parton dynamics [39, 40]. If the forward jet has large energy ($x_{jet} = E_{jet}/E_{proton} \gg x_{Bj}$) the evolution from x_{jet} to small Bjorken-x can be studied. When the transverse energy of the jet is of the same order as Q^2, $E_T^2 \sim Q^2$, there is no room for Q^2 evolution and the DGLAP formalism predicts a rather small cross section in contrast to the BFKL/CCFM/LDC formalisms, which describe the evolution in x. Measurements [41, 42] performed in the first phase of HERA running show that the prediction from the naive DGLAP formalism lies a factor ~ 2 below the data, whereas the data can be described by the CCFM or LDC evolution equations [43], provided the non-singular terms are not included in the parton splitting functions.

Typical event selection criteria were:

$$
\begin{aligned}
&Q^2 > 5\ \mathrm{GeV}^2 \\
&E_{t\ jet} > 3.5\ \mathrm{GeV} \\
&1.7 < \eta_{jet} < 2.7 \\
&x_{jet} > 0.035 \\
&0.5 < E_T^2/Q^2 < 2
\end{aligned}
$$

In the rapidity range covered by the present HERA experiments the forward jet cross section is, however, also reasonably well described by the DGLAP model, including a resolved virtual photon contribution and when a sufficient lever arm is allowed for the evolution of the resolved photon.

The measurements at HERA were mainly restricted by two factors: the available center-of-mass energy and the geometrical acceptance of the detectors, requiring the forward jet to lie between: $2 \lesssim \eta \lesssim 3$. In Fig. 8 the forward jet cross section is shown as a function of x_{Bj} in a larger rapidity range up to $\eta_{jet} < 6$. The Color Dipole Model (CDM) as implemented in ARIADNE [44] [1], a standard DGLAP(LEPTO [46]) and the CCFM(CASCADE [47]) models predict rather large cross sections, the difference compared to DGLAP getting more significant with increasing rapidity.

As mentioned before, the CCFM and the LDC models give a good description of the present forward jet measurements, provided only the singular terms are included in the splitting function. All attempts so far to include the full splitting function all give a worse description of the measurement. Is there a dynamical mechanism which suppresses the non-singular terms in the splitting functions, or increases the effective lever arm in the evolution of the resolved photon? Or is a completely new mechanism at work? Only an extended study of exclusive final state properties over the full range of rapidities up to the proton provide the data which may lead to the answers.

Further measurements in the forward region With very forward detectors one could study the transition region from diffractive to non-diffractive events. This is very important for discriminating between different models for diffraction. In Pomeron (or Regge based) models the leading proton (neutron) is equivalent to the

[1] using the tuned parameters given by 'set2' in [45]

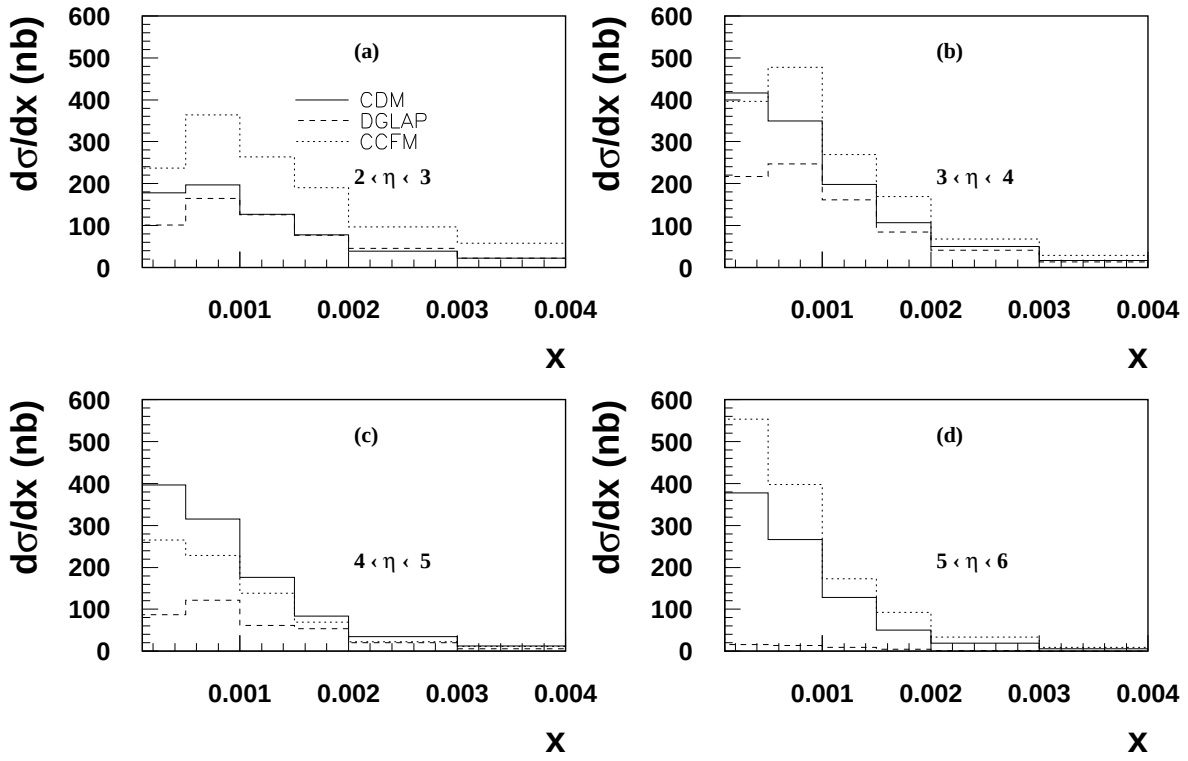

Figure 8: Forward-jet cross section as a function of x obtained from the CDM (ARIADNE), DGLAP (LEPTO) and CCFM (CASCADE) models. The forward jet is required to be in the angular region of (a): $2 < \eta < 3$, (b): $3 < \eta < 4$, (c): $4 < \eta < 5$, (d): $5 < \eta < 6$.

colliding proton by construction whereas in Soft Color Interaction (SCI) -type models one has a small mass system which will then fragment into a leading baryon with or without accompanying hadrons. The models are now tuned to fit available data, but perform rather differently in the as yet unobserved intermediate region. This, of course, relates to the more general problem of hadronization and confinement.

Strangeness - production The measurement of strangeness production will play a key role to answer questions raised about jet universality and the QCD vacuum. In Fig. 9 we show the K^0 and Λ production as a function of rapidity η as predicted by different models in the range of $0.25 < p_t^2 < 4.5$ GeV^2, $10 < Q^2 < 79$ GeV^2, $10^{-4} < x < 10^{-2}$ and $0.05 < y < 0.6$. The range covered by present HERA measurements is restricted to $\eta \lesssim 1.5$, but huge differences not only in rate but also in shape are predicted in the range $2 < \eta < 6$. In order to draw conclusions, the whole η range needs to be measured and understood.

Baryon production The universality of fragmentation can also be investigated by measuring baryon production as a function of rapidity. As argued above, in the central rapidity region, the fragmentation ought to be known from e^+e^-. When moving towards the fragmentation region of the colliding hadron, an increasing influence of the valence quarks should be visible. In Fig. $10(a-b)$ the rate of baryon(p) and anti-baryon ($\bar{p}$) production is shown as a function of the rapidity in the laboratory frame. One can see that in the central region

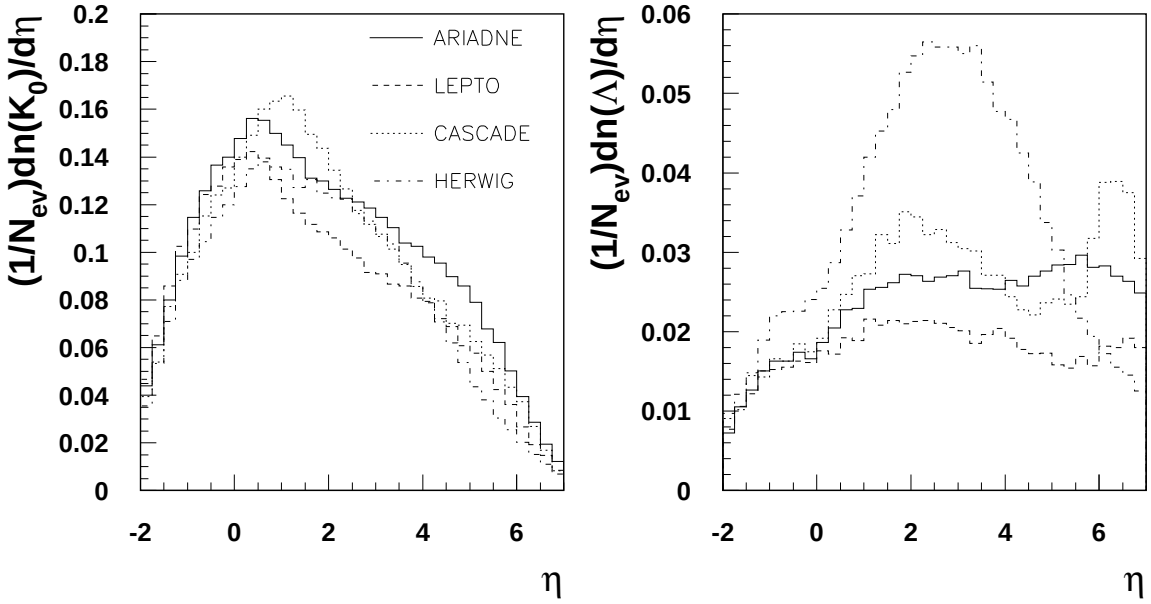

Figure 9: Predicted η spectrum for K^0 (left) and Λ (right) production in the range $0.25 < p_t^2 < 4.5$ GeV^2, $10 < Q^2 < 79$ GeV^2, $10^{-4} < x < 10^{-2}$ and $0.05 < y < 0.6$ compared with predictions from ARIADNE, LEPTO, HERWIG and CASCADE.

of rapidity in the HERA laboratory frame ($-1 < \eta < 2$), both models give similar results, whereas in the region closer to the colliding proton ($3 < \eta < 6$), differences close to a factor of two are observable.

The intrinsic k_t distribution of the partons inside the colliding hadron can be measured by the leading baryon in the rapidity range of $5 < \eta < 6.5$. Different MC models predict very different distributions. The k_t distribution of the remnant should not only be viewed as an inclusive quantity, but in the context of k_t correlations. Given a net p_T imbalance in the central region, how much of the recoil is taken by the proton remnant and how much by other "minijets" in the proton fragmentation region? It will be interesting also to measure the intrinsic k_t distributions inside the proton and neutron separately, in order to verify the universality of the Fermi motion and QCD effects. The transverse momentum of a leading proton in the p-fragmentation region is shown for two different QCD models in the right-hand plot of Fig. 10.

2.3.4 Heavy quarks

We also propose to study final states including the heavy quark (HQ) charm (c) or beauty (b) with future HERA running. The large masses of the HQs provide a "hard" scale needed to compare the data with QCD predictions. The main objectives are to perform precise tests of QCD dynamics in kinematic regions never accessed before, namely in the very forward pseudorapidity, η, regions and in the transition region between photoproduction (PHP) and deep inelastic scattering (DIS), i.e. Q^2 between 0.5 and 5 GeV^2. Recent results on c production in γp collisions and b production in $p\bar{p}$, γp and $\gamma\gamma$ collisions disagree with QCD next-to-leading order (NLO) calculations. More precise measurements and improved calculations are required to understand the origin of this disagreement and to find out if this is due to the lack of higher order corrections to existing theories or to a possible source of "new physics".

NLO calculations are currently available for comparison with measurements of HQ PHP at HERA: (1) A

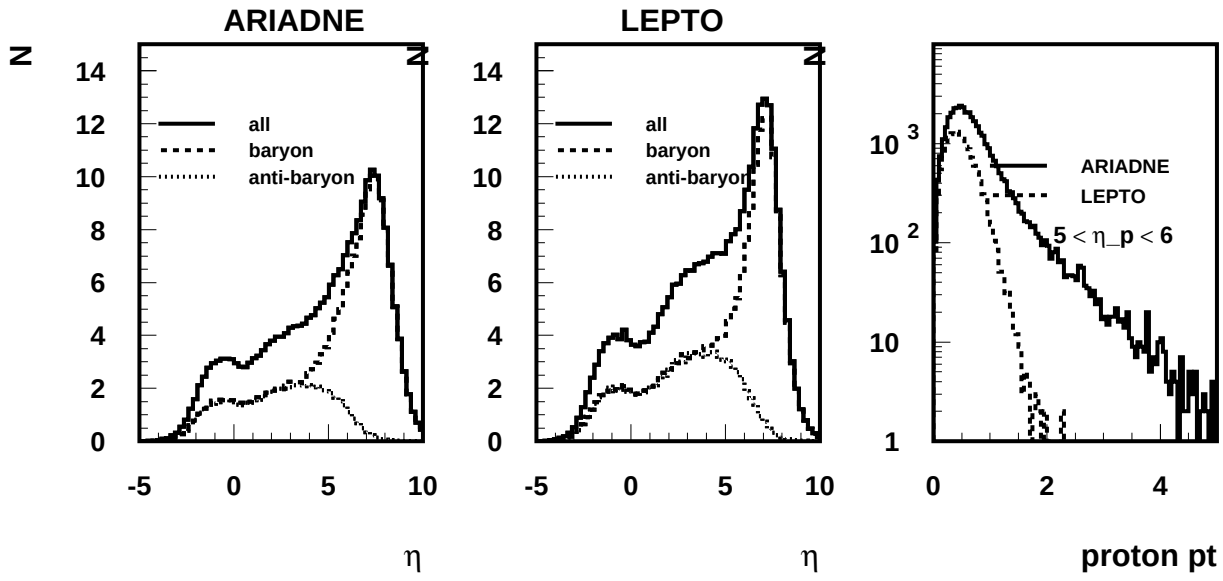

Figure 10: Rate of baryon production as a function of rapidity for $Q^2 > 5$ GeV^2. Shown are the predictions from the ARIADNE and LEPTO MC generators. In the right hand plot, the p_t distribution of leading baryons in the range $5 < \eta < 6$ is shown.

fixed-order ("massive") approach [48], where HQs are produced only dynamically in the hard subprocess. (2) A resummed ("massless") approach [49], where (massless) HQs are assumed to be in the photon and proton parton distributions and interact in the hard subprocess. Recently, fixed-order plus next-to-leading-logarithmic (FONLL) calculations for charm photoproduction at HERA and b production in the Tevatron have become available [50, 51]. These calculations incorporate mass effects up to NLO and the resummation of transverse-momentum logarithms up to NLL level, and are supposed to be valid at both low and high p_T^2.

The ZEUS collaboration has preliminary results [52] on D^* photoproduction, in which single and double differential cross-sections have been compared to the above mentioned NLO calculations (see for example Fig. 11). None of the above calculations are able to describe the measured data satisfactorily. Furthermore, even though the theoretical uncertainties are large, it is clear that the main disagreement occurs in the forward η region, in particular for medium p_T values. Hence, in order to obtain a better insight into this discrepancy, it is essential to push the measurements in the forward direction and get to η regions inaccessible so far. An extension of the tracking up to $\eta \approx 5.0$ will enable the reconstruction of charm hadrons in the forward direction and will increase the number of D^*s by about a factor of 2.4 (Fig. 12). There are also outstanding discrepancies between data [53] and theoretical expectations [54] for b hadron production. An extension of the kinematic regime could pinpoint where the discrepancies set in.

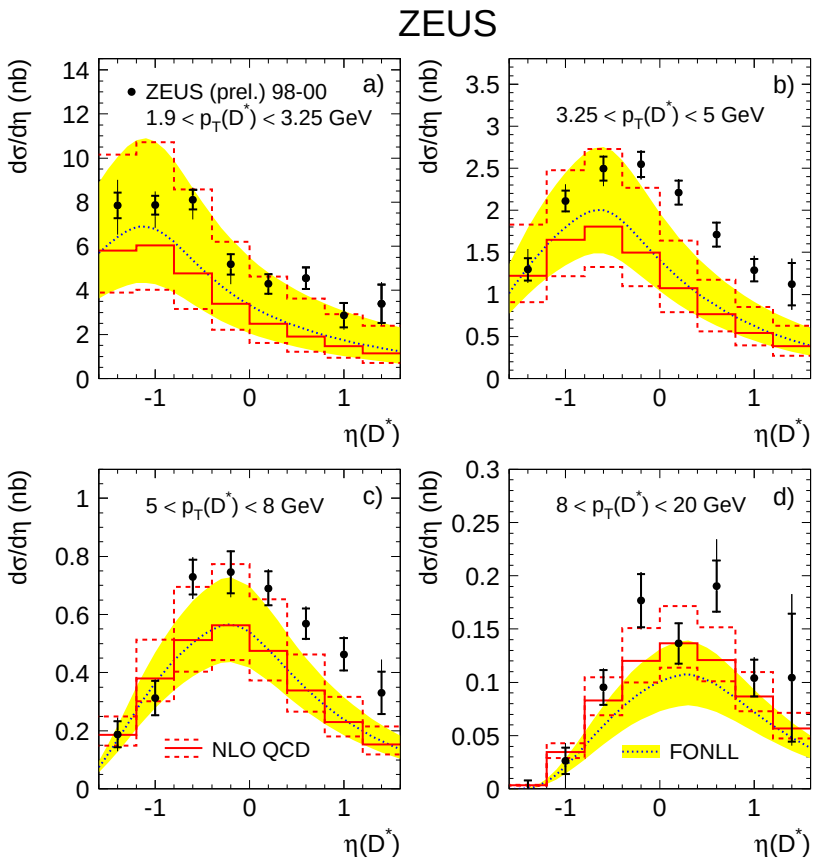

Figure 11: Differential cross sections $d\sigma/d\eta$ for inclusive $D^{*\pm}$ photoproduction in the process $ep \to D^{*\pm}X$ for various $p_T(D^*)$ regions. The inner error bars show the statistical uncertainty and the outer ones show statistical and systematic uncertainties added in quadrature. The predictions of NLO calculations with a nominal choice of parameters are given by the solid histograms. The dashed histograms correspond to the upper and lower bounds of the predictions. FONLL predictions are shown as dotted curves and their uncertainties are given by the shaded bands.

2.4 Electron nucleus scattering

Using HERA as an electron ion collider offers unique possibilities to test completely new features and long-standing problems of perturbative QCD. The extremely high center-of-mass energy of HERA makes this the ideal laboratory to explore the very low x physics where shadowing and saturation effects are expected to be present. Measurements on deuterons and at least one heavy nucleus are needed to reach that goal.

2.4.1 Nuclear Effects in Parton Distributions

Since the discovery of the EMC effect [55], parton distributions are known to be modified in the nuclear medium compared to the free nucleon case. Subsequent experiments have measured the $x-$, Q^2- and A-dependence of the nuclear effects in deep-inelastic scattering with high precision [56]. However, the interpretation of these data is far from unique: as inclusive charged lepton deep inelastic scattering probes the gluon distribution only indirectly through the Q^2 evolution of the measured structure functions, the observed shadowing in the nuclear structure function can be modeled by different combinations of quark and gluon distributions in the nucleus. As an example, an analysis of the most precise data available, the NMC measurement of F_2^{Sn}/F_2^C [57], resulted in a possible enhancement of the gluon distribution in Sn compared to that in C at intermediate x values of up

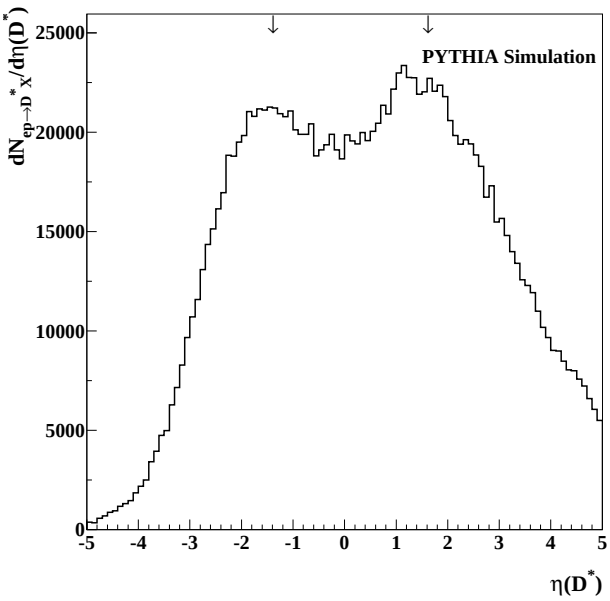

Figure 12: The D^* distribution in η calculated at generator level in PYTHIA Monte Carlo, for η regions between -5.0 and 5.0. The ratio of events between $0 < \eta < 5.0$ and $0 < \eta < 1.6$ is 2.4. Arrows are the HERA I tracking acceptance.

to 40% [58].

At the extremely high center-of-mass energy of the HERA collider with the option to accelerate light and heavy nuclei, measurements of structure function ratios on a nucleus A with respect to deuterium could improve our knowledge of these medium modifications significantly. Of special importance here is the extension of the measurement to low values of x over a large Q^2 range. All previous measurements of nuclear shadowing have been obtained at fixed target experiments, resulting in relatively low values of Q^2 at low values of x, especially in Q^2 values well below 1 GeV^2 in the most interesting range of $x < 10^{-3}$ where the gluon distribution in the free nucleon dominates. An indication of the large resulting uncertainties in the nuclear parton distributions is shown in Fig. 13 where the estimates from two different analyses are shown. Because of the large Q^2 range at low x these uncertainties should be essentially eliminated at HERA even with moderate luminosities.

In the shadowing region easily accessible at HERA the question of nuclear modifications to the parton distributions is believed to be very closely related to diffrative scattering. More recently, it was suggested [61] that this relation might be even more fundamental and one manifestation of the influence of the QCD gauge links on the parton distributions. In this view shadowing is not intrinsic to the wave function of the nucleon, but is a coherent effect arising from the destructive interference of diffractive channels induced by final state interactions. Gluon exchange between the fast outgoing quarks and the target spectators, which is usually assumed to be an irrelevant gauge artefact, affects the leading twist structure functions and might partially destroy the usual relation between the deep inelastic scattering cross section and the parton probabilities of the initial state. If this approach is correct, it might lead to differences in shadowing probed by charged and neutral currents – possibly even explaining the old standing difference between neutrino and charged lepton deep inelastic scattering data on iron. Because of the high energies of HERA this hypothesis should be testable within one experiment.

Besides the inclusive studies described above, the HERA collider will allow a detailed study of the nuclear dependence of diffractive processes and jet production. Both processes are sensitive to the gluon distribution in the nucleus. Additionally, charm production and the longitudinal structure function will give independent measurements of the gluon density in nuclei. Understanding the origin of shadowing is of the highest importance for the interpretation of any high-energy process involving nuclei. Shadowing influences the final state particle multiplicities and energy densities in relativistic heavy ion collisions, results in opacity effects that can mask

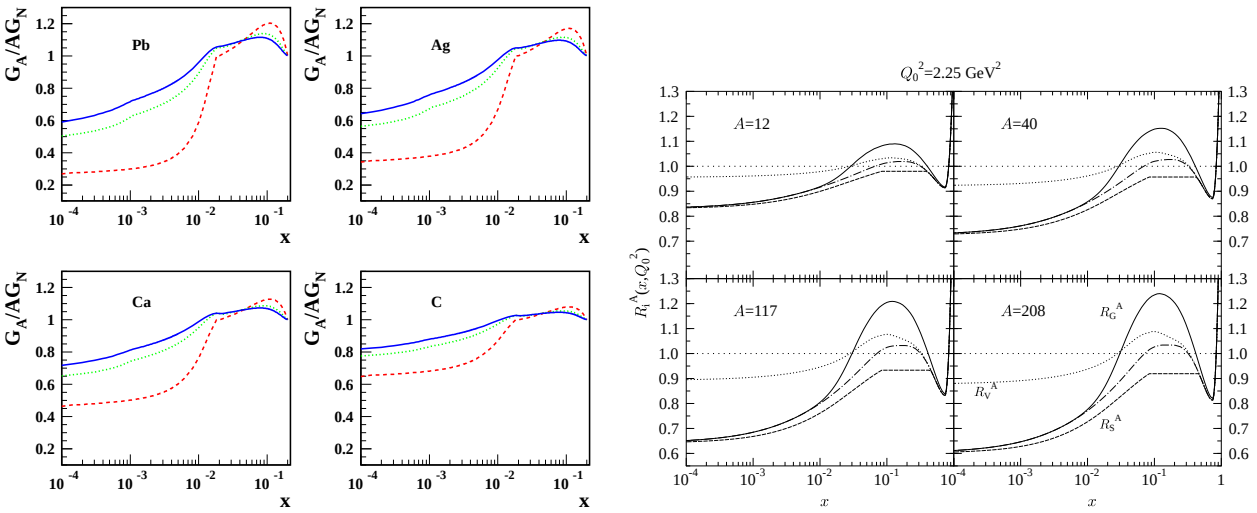

Figure 13: Shadowing of parton distributions in different nuclei: (left) for the gluon distribution at different Q^2 values of 4,25,100 GeV^2 (red,green,blue) [59]; (right) for valence quarks, sea quarks and gluons at Q^2=2.25 GeV^2 [60].

color transparency in vector meson production and limits the present ability to calculate partonic energy loss in the nuclear medium.

2.4.2 High Density Partonic Matter

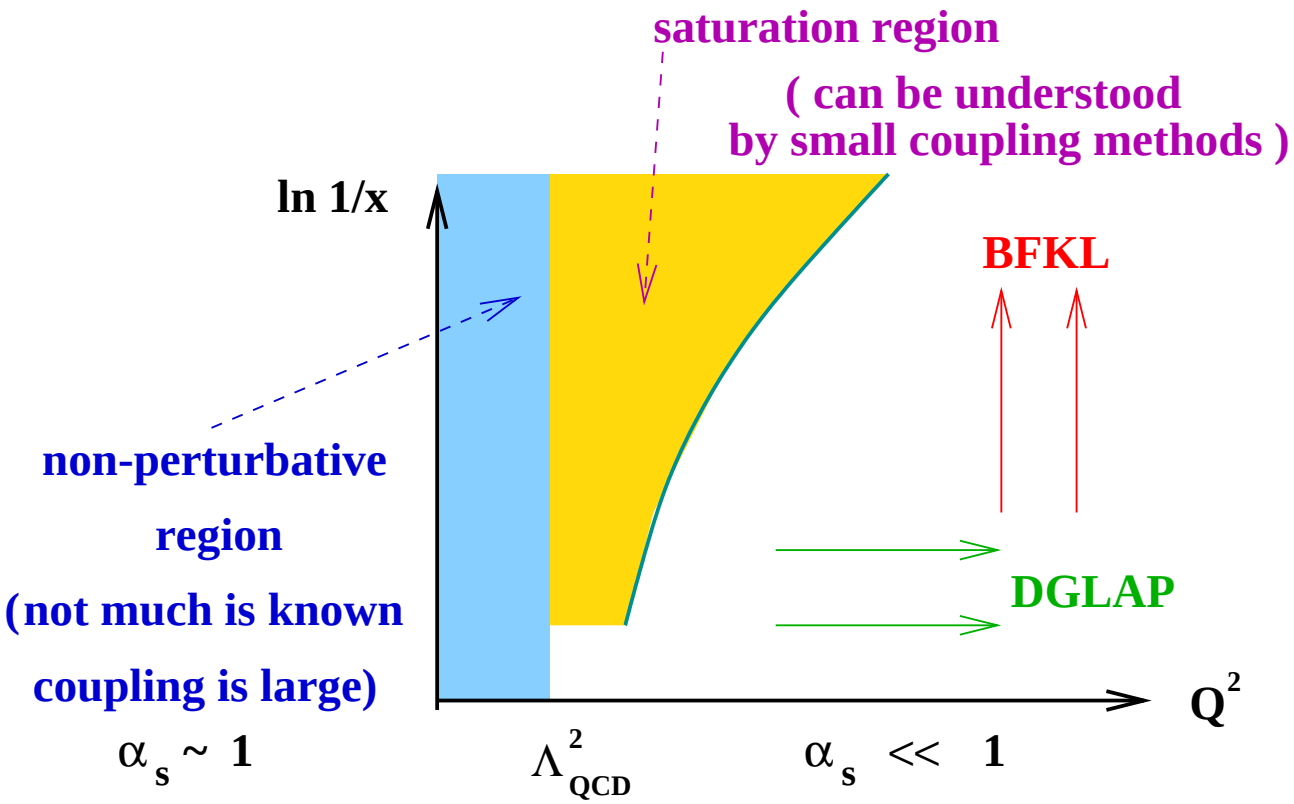

Figure 14: Schematic view of the $ln(1/x) - Q^2$ plane showing the regimes of applicability of different evolution equations

The very high center-of-mass energy of the HERA collider presents a unique opportunity to study a very fundamental aspect of QCD. As one goes to higher energies, the density of small x partons grows as $x^{-\delta}$ with $\delta \sim 0.3$ for Q^2 values of a few GeV^2. As a high energy probe simultaneously resolves partons from different nucleons along its trajectory, this density also grows as $A^{1/3}$. The nucleus thus acts as an amplifier for the novel physics expected at high parton densities - aspects of QCD which otherwise could only be explored in an electron-proton collider with energies well above those of the HERA collider. The density per unit rapidity associated with these partons is $Q_S^2 \propto A^{1/3}x^{-\delta}$. If Q_S is big enough, the strong interaction is expected to become a weak interaction ($\alpha_S << 1$) and thus a scale invariant theory. In this limit, many features of multi-particle production can be computed from first principles. Figure 14 shows a schematic view of the ln(1/x) and ln(Q^2/Λ^2) plane. In the region of either high Q^2 or large x where the density of partons is moderate, the evolution of parton densities with respect to Q^2 or $\ln(1/x)$ is usually described by the DGLAP or BFKL evolution equations. Evolving into the high parton density regime (yellow area), these linear evolution equations should get corrections resulting in a moderation or even saturation of the growth of the parton densities. Experimentally, there is evidence from pA experiments at Fermilab that the typical momenta of partons increases as $p_T^2 \sim Q_S^2$. There are also hints from HERA that one may be beginning to see high parton density effects at Q^2 values around 1-10 GeV^2 and the lowest available values of x. Phenomenological models that contain a saturation scale $Q_S^2 \sim 1$ GeV^2 at $x \sim 10^{-4}$ [62] have been successful in explaining the HERA inclusive, diffractive and vector meson production data. More recently, lattice calculations including saturation effects from nonlinear perturbative QCD have shown similar agreement with the HERA low x data [63] (Fig. 15). The same data can however also be described without any saturation effects. Using a heavy nucleus as an amplifier should make the experimental detection of this new feature of QCD unambiguous.

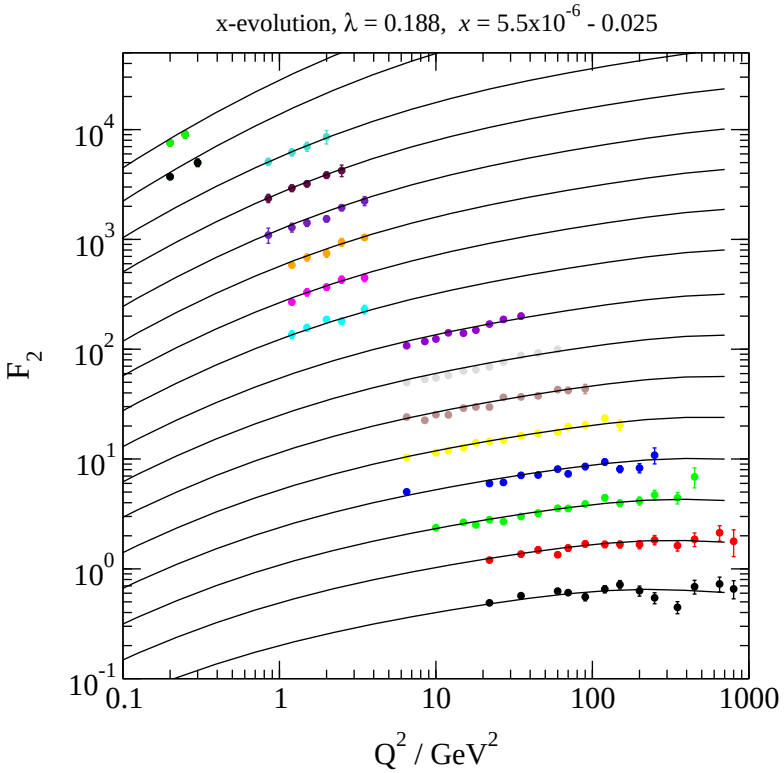

Figure 15: The low x data from HERA ep scattering in comparison to a lattice calculation including saturation from nonlinear pQCD

A number of inclusive and semi-inclusive observables are expected to be sensitive to the effects of high parton densities. As already mentioned, the structure function $F_2(x, Q^2)$ and its logarithmic derivative can be measured with high accuracy. Corrections due to high parton densities will result in deviations from pQCD

fits incorporating the standard DGLAP evolution. The same feature is expected in the longitudinal structure function $F_L = F_2 - 2xF_1$. The ratio of the longitudinal to transverse structure functions is expected to show a maximum at a particular Q^2 related to the saturation scale Q_S^2. Other quantities sensitive to high parton density effects include the fraction of diffractive events and the cross section for coherent vector meson production.

2.4.3 Relation to Heavy Ion Collisions

The new measurements possible with eA collisions at HERA are essential for a fundamental understanding of relativistic heavy ion collisions. Experiments to study QCD at high temperature and density using such collisions are underway at the new Relativistic Heavy Ion Collider (RHIC) at Brookhaven National Laboratory, and planned at the Large Hadron Collider at CERN.

Unambiguous conclusions from complicated hard scattering between hundreds of bound nucleons at high energies demands determination of presently unmeasured parton distributions in nuclei. In particular, the parton distributions in the initial nuclei constitute the initial state for this relativistic collision. A new round of experimentation at HERA with nuclear projectiles could determine these distributions over a large kinematic range for the first time. Already, there are tantalizing hints from RHIC data [64] that the gluon distribution at low x in the initial nuclei may indicate saturation. Figure 16 shows the measured scaled pseudorapidity distribution as a function of the number of participants in gold-gold collisions at center-of-mass energies of 130 and 200 GeV. The data are consistent with a saturation model constrained by HERA data. However, there are other less exotic explanations which also explain the data. It is very unlikely that this can be resolved by heavy ion experiments. Electron-nucleus collisions at HERA could confront this issue directly at low-x.

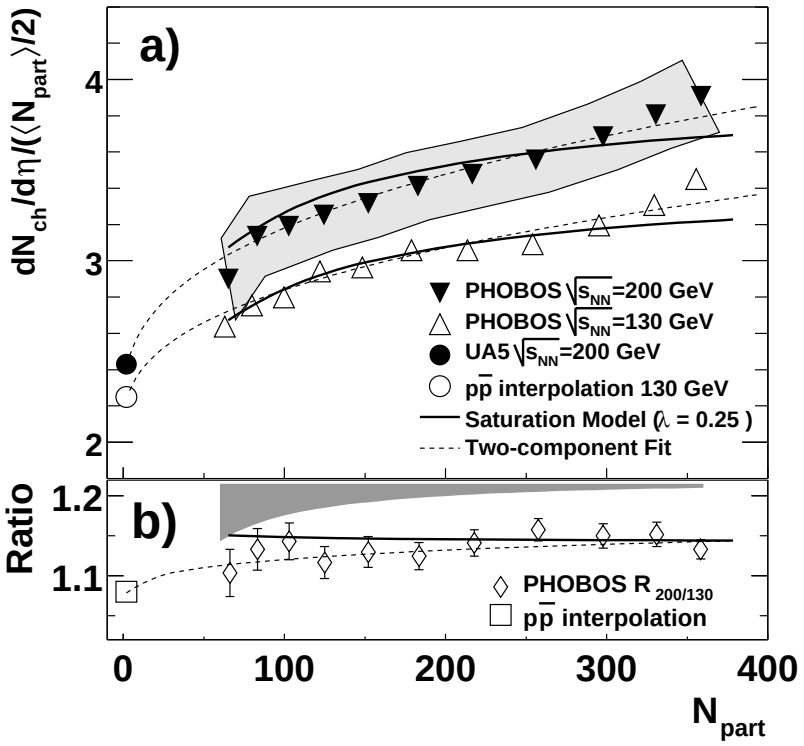

Figure 16: Midrapidity $dN/d\eta$ per participant pair versus centrality at 130 and 200 GeV from the Phobos experiment. Models, pp data, and 200/130 ratios also shown.

In addition to measuring the fundamental parton distributions in nuclei, such new experiments could probe many processes involving partons in nuclei which are central to disentangling the complicated relativistic heavy ion collisions. Parton energy loss and fragmentation in nuclei are two issues with profound consequence for

interpreting the present RHIC data which can only be directly probed by HERA using the precision of the electromagnetic probe and the unique charcteristics of the HERA experimental configuration.

2.4.4 Other Subjects

Besides the three main subjects outlined above, several other important aspects of perturbative QCD and nuclear modifications of universal quantities can be adressed by lepton-nucleus interactions at HERA. These include (with no attempt to be complete)

- Colour Transparency
  At high enough Q^2 colour transparency (CT) is expected in perturbative QCD. Experimental evidence is however rather scarce: in the cleanest channel, $ee' p$, no evidence for CT has been found in carbon or iron for Q^2 values up to 8 GeV^2; exclusive vector meson production shows some indication but suffers from statistical precision and – more importantly – from a sufficient range in ν (or coherence length) and Q^2. The large kinematic range of HERA will allow to settle this subject.

- Deeply Virtual Compton Scattering (DVCS) in nuclei
  First measurements of DVCS in nuclei seem to indicate that this process is observable in the nuclear environment. Even though the interpretation presently is not at all clear, the implication for building generalised parton distributions and testing their universality present interesting possibilities in this new field of perturbative QCD.

- Tagged Structure Functions
  Tagged structure functions are believed to help disentangle the effects of the nuclear medium. Even though their primary importance is probably in the region of high x, the unambigious identification of the scattered nucleon will also help understand the effects of shadowing, especially in case of deuterium. Replacing the proton with deuterons would also allow to test the independence of QCD radiation to the initial parton at small x. At large x, the flavor dependence of the parton densities could be sorted out.

2.4.5 Luminosity and Detector Requirements

For most of the processes discussed above, only moderate luminosities are needed. To reach these, cooling of the ion beam is however absolutely essential. Two possibilities for such cooling have been discussed: electron cooling which has been demonstrated to work at lower energies but needs to be developed for the extremely high energy envisioned for HERA. Secondly, laser cooling has been suggested as an alternative. Both techniques require significant R&D.

Both a modified H1 detector (including a tagger for the “recoiling” protons or neutrons) and/or a new detector optimised for the measurement of diffractive events and low Q^2 physics would allow to perform these measurements.

2.5 Summary of measurements and requirements

2.5.1 Summary of measurements

In summary, we see the following measurements as the highlights of the proposed program:

- The measurement of the longitudinal structure function, F_L, particularly at Q^2 values below 10 GeV^2, where present theoretical and experimental uncertainties are very large.
- The measurement of F_2 from $Q^2 = 0.1$ GeV^2 to $Q^2 = 10$ GeV^2 with high precision, to better understand the observed transition of the cross sections from partonic to hadronic behavior.
- The measurement of diffractive and exclusive reactions (VM production and DVCS) over the full W range, and to values of $|t| \leq 1.5$ GeV^2, with no proton dissociation background, to perform a three dimensional mapping of the proton and perform first extractions of generalized parton distributions.
- The measurement of forward jets and forward particle production up to pseudorapidities of $\eta = 6$ to test in a direct way our understanding of parton branching in strong interactions and to see the onset of collective phenomena. Acceptance for forward jets will also allow the measurement of F_2 to $x = 1$ at moderate Q^2.

All of the above measurements should be performed with protons and with at least two nuclear targets (e.g., deuterons and Hg nuclei), to search for the gluon condensate, and understand nuclear effects in parton distributions.

2.5.2 Accelerator requirements

The luminosity requirements for the eP program are set by exclusive cross section measurements at high t, F_2 measurements near $x = 1$, and by the F_L measurement. We anticipate requiring data sets with three different proton energy settings ($E_P = 460, 690, 920$ GeV). A luminosity requirement of approximately 50 pb^{-1} at each energy is anticipated, but a detailed optimization is yet to be worked out. The luminosity required for the *eA* program has been estimated at 2 pb^{-1} per nucleon [65]. We do not anticipate needing electron beams - positron beams will suffice - since we are concerned primarily with the Q^2 region where photon exchange dominates.

Beam polarization would of course be very desireable, and would allow for a broadened physics program. It is however not considered a necessity for this proposal.

2.5.3 Detector requirements

The main focus of the design of a new detector is the extension of the angular coverage compared with the existing H1 and ZEUS detectors, in both the electron and proton directions. In the electron direction, particular attention must be placed on the measurement of F_L and F_2 at small Q^2 ($0.1 < Q^2 < 10$ GeV^2). This requires to track and identify the scattered positrons with energies between 2 GeV and 27.5 GeV up to high rapidities.

The extension of the rapidity range can be facilitated by a dipole field that separates scattered positrons from the beam. The determination of the kinematic properties of the positrons and their identification require for the positron hemisphere:

- high precision tracking with
  - $\Delta p/p$ of $\leq$2 %
  - angular coverage down to a pseudo-rapidity of $\approx$-6 over the full energy range
- em calorimetry with
  - an energy resolution of better than $\approx 20\ \%\ \sqrt{E}$

  - e-π separation with a pion rejection factor of at least 20 at 90 % efficiency over a positron energy range from 2 GeV to the beam energy of 27.5 GeV.

Another focus of the detector program is the study of forward jets, high-x events, and exclusive processes. This leads to the following additional requirements for the proton hemisphere:

- high precision tracking with
  - similar precision in the proton hemisphere as in the positron hemisphere
  - similar angular coverage up to a pseudo-rapidity of $\approx$6
- em and hadronic calorimetry in the proton hemisphere with
  - an em energy resolution of better than $\approx$20 % $\sqrt{E}$
  - a hadron energy resolution of better than $\approx$50 % $\sqrt{E}$
  - e-π separation with a pion rejection factor of at least 10 at 90 % efficiency above 2 GeV energy.

3 A new detector for HERA

3.1 Detector concept

The main idea is to build a compact detector with tracking and central em calorimetry inside a magnetic dipole field and calorimetric end-walls outside. The detector inside the magnet[s] should not exceed a radius of 80 cm. The coordinate system has the z-axis parallel to the proton beam, the x-axis horizontal and the y-axis vertical. The positrons thus point towards negative z.

The tracking focuses on the forward and backward tracks. The calorimetry is to show the best performance in the central region where momentum measurements are intrinsically less precise due to the field configuration and thus e-π separation more difficult. Tracking for $|\eta| < 0.5$ is not currently foreseen.

3.1.1 Magnets and Beam-Line

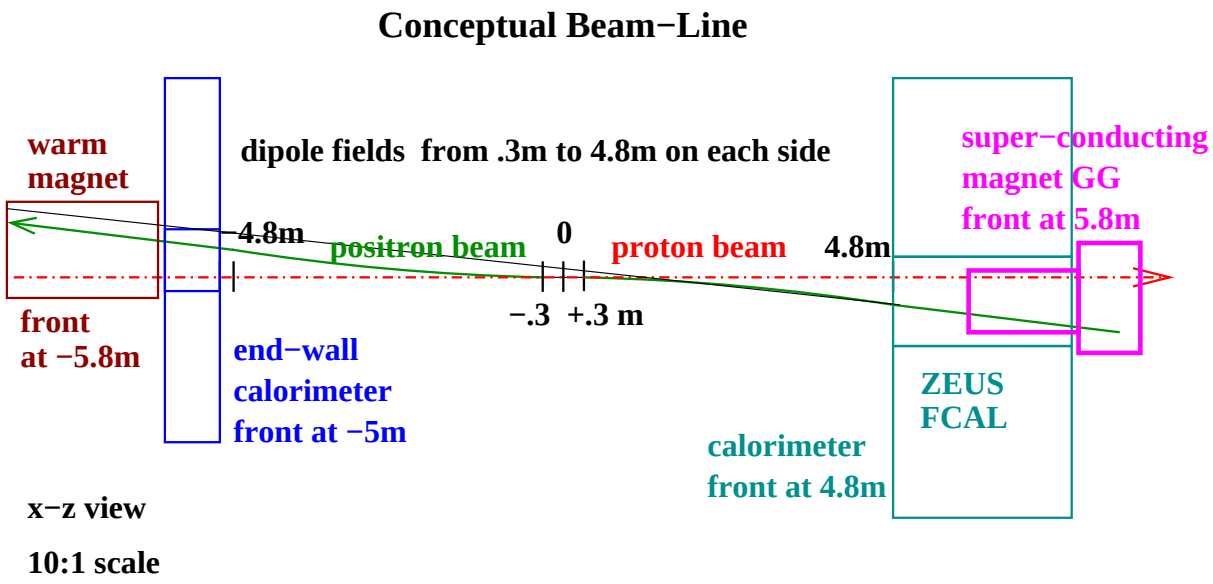

Figure 17: Possible arrangement of elements around the interaction point.

The local strength and the integrated field of the magnets are restricted by beam considerations like the synchrotron radiation produced. In general longer magnets with lower fields are preferred over shorter and stronger magnets. However, the detector cannot be unrestrictedly long, because luminosity considerations require that the first machine elements be placed at approximately 6 m from the interaction point.

A single long dipole field does not seem feasible, as the resulting synchrotron fan would be extremely wide and the masking of back-scattered synchrotron radiation would be difficult. The baseline design therefore assumes a magnetic field $+B_y$ in the positive z hemisphere and $-B_y$ in the negative z hemisphere. The resulting synchrotron fan is confined to the positron side of the beam-pipe and the masking becomes more efficient due to favorable angles. The split magnetic field as described above is not physically possible. However, it is used in all simulations, extending to ± 4.5 m with a strength of 0.3 T.

The final magnet system will most likely have a field free central region somewhat matched to the size of the interaction region. The expected change in basic performance is small, especially for the forward regions on which the design focuses.

Figure 17 shows a possible layout [1] of the interaction region using existing magnets. In this x-z view the x-axis is scaled up by a factor of 10. A field free region of ± 0.3m is assumed. The 0.3 T fields extend to 4.8 m on each side. In -z, the positron hemisphere, the calorimeter end-wall starts at 5 m and is .8 m thick, allowing

[1] Special thanks to Ferdinand Willeke and Uwe Schneekloth for their work on this subject.

the use of the warm magnetic quadrupoles from either the HERA-I or HERA-II configuration to be placed at 5.8 m. These magnets have enough aperture to contain the two beams and the synchrotron radiation fan at this location.

On the +z side, the proton hemisphere, the situation is more complicated due to the space requirements of a hadronic calorimeter. However, it seems possible to use one of the very compact super-conducting magnets from the ZEUS Hera-II setup. Their outer diameter of less than 20 cm makes it possible to insert them into the calorimetric end-wall without a large loss of acceptance. The GG-magnet from the HERA-II interaction region has the needed aperture when placed at the HERA-I position of 5.8 m. The ZEUS FCAL calorimeter is taken as an example calorimeter for this end-wall. The energy resolution is certainly adequate for our needs, but a finer granularity would likely be needed, particularly near the beam-line. In Fig. 17 it is placed at 4.8 m and the GG-magnet from the HERA-II interaction region is placed inside.

The scenario described here seems satisfactory, although a lot of detailed studies will be needed. It should be noted that the synchrotron load from the central dipole magnets would be 22 kW per magnet. Good masking will be essential. In addition detailed studies of beam-gas backgrounds will be needed.

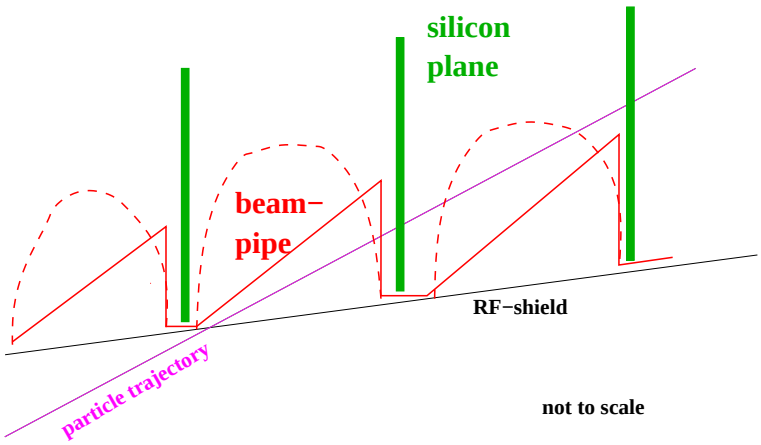

Figure 18: Possible schematic beam-pipe designs to minimize the impact of the material in the beam-pipe on the particle trajectories. The solid red line depicts an opening of the beam-pipe in front of each plane; the dashed indicates another option considered.

3.1.2 Beam-Pipe

The simulated design contains a beam-pipe that has a fixed radius of 3 cm vertically and opens up conically in the horizontal direction. It is later depicted in Fig. 19 together with the tracking system. At the interaction point the horizontal width of the pipe is ± 3 cm and it opens up by 1.5 cm per meter in z on both +x and -x. This keeps the deflected electron beam at least 3 cm away from the wall of the beam-pipe and should contain the synchrotron fan (the actual beam-pipe design will depend critically on the magnetic field configuration chosen). In the current simulation, the beam-pipe also opens in +z, and the beam-pipe consists of 0.5 mm aluminium. This is not quite realistic for such a large beam-pipe. The material in the beam-pipe will have to be optimized, because the forward particles traverse the pipe at a shallow angle. Two possible design options are depicted in Fig. 18. These types of designs introduce the additional complication of RF-shielding. Most likely a beam-pipe like this will only be needed towards the ends of the detector.

Contrary to the simulated beam-pipe, the final beam-pipe will be asymmetric in x. Its opening will be adjusted to the apertures of the beam magnets at 5.8 m, see Fig.17. As beam-gas events will be a severe background, the quality of the vacuum will be of utmost importance. Therefore we envision to integrate ion-getter-pumps into the beam-pipe. They would be placed on either the +x or the -x side of the beam-pipe and would take up approximately 4×4 cm^2 in the x-y plane. Acceptance studies will determine which side is

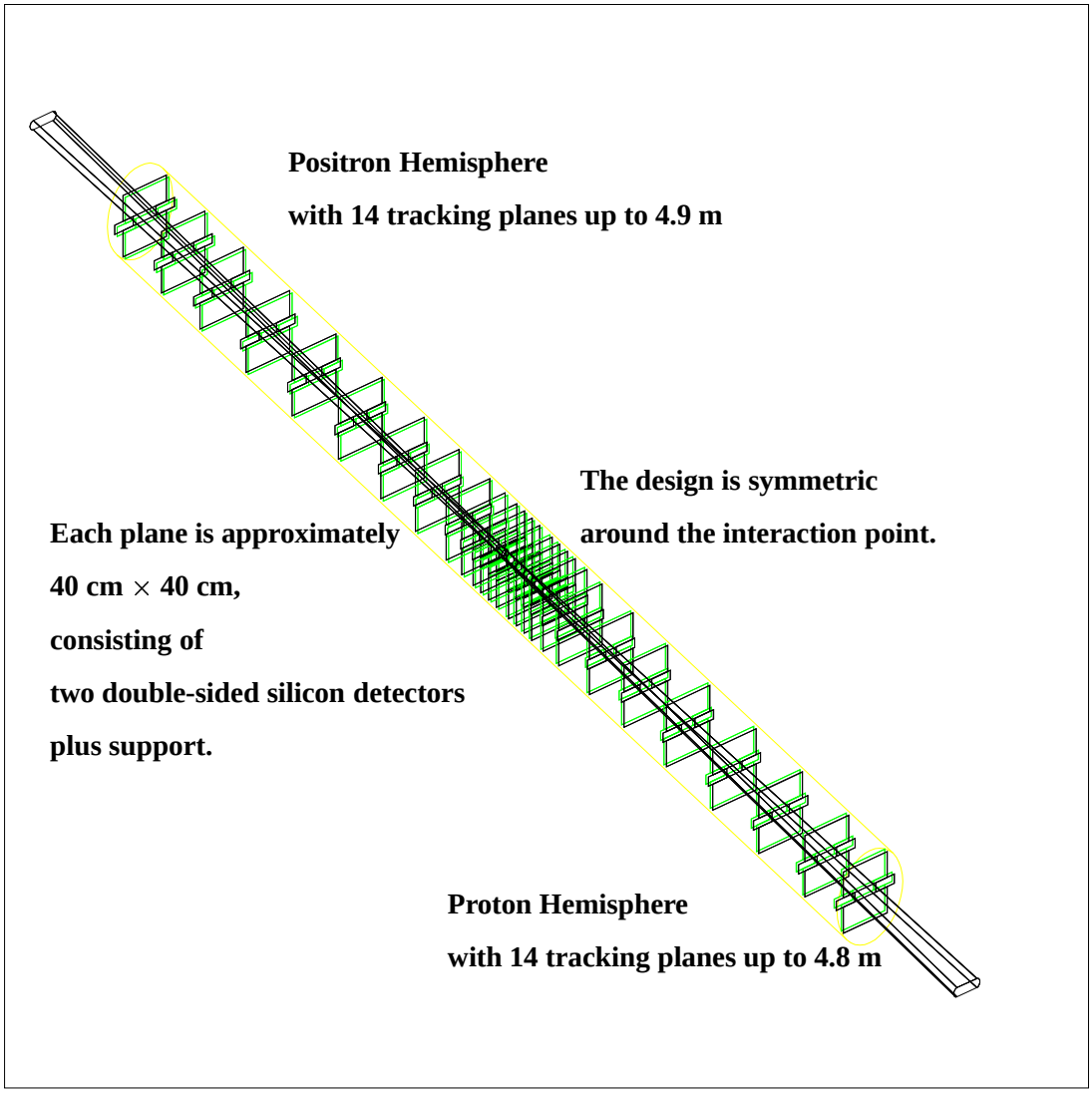

Figure 19: Overview over the silicon tracker. The system is confined to cylinder with a radius of 30 cm. Also visible is the widening beam-pipe.

favorable.

3.1.3 Tracking System

The precision tracking required translates into hit resolutions of less than about 50 μm. This makes silicon strip detectors an obvious choice of technology. As the material budget will be important, double-sided detectors are desirable. A read-out-pitch between 50 μm and 100 μm will be adequate. Two double-sided detectors with appropriate stereo angle design can yield unambiguous space-points. For the baseline design we assume silicon tracking stations with two double-sided, 300 μ thick silicon strip detectors and support structures with material equivalent to 1.2 mm of carbon fiber. This results in stations with a material budget equivalent to $\approx$1 % of a radiation length X_0.

The complete tracker is composed of planes oriented perpendicular to the beam. The planes are centered around the proton beam line and measure approximately 40×40 cm^2. They have a central cut-out that follows the beam-pipe design. Each plane is composed of a top and a bottom half and two horizontal plugs that are

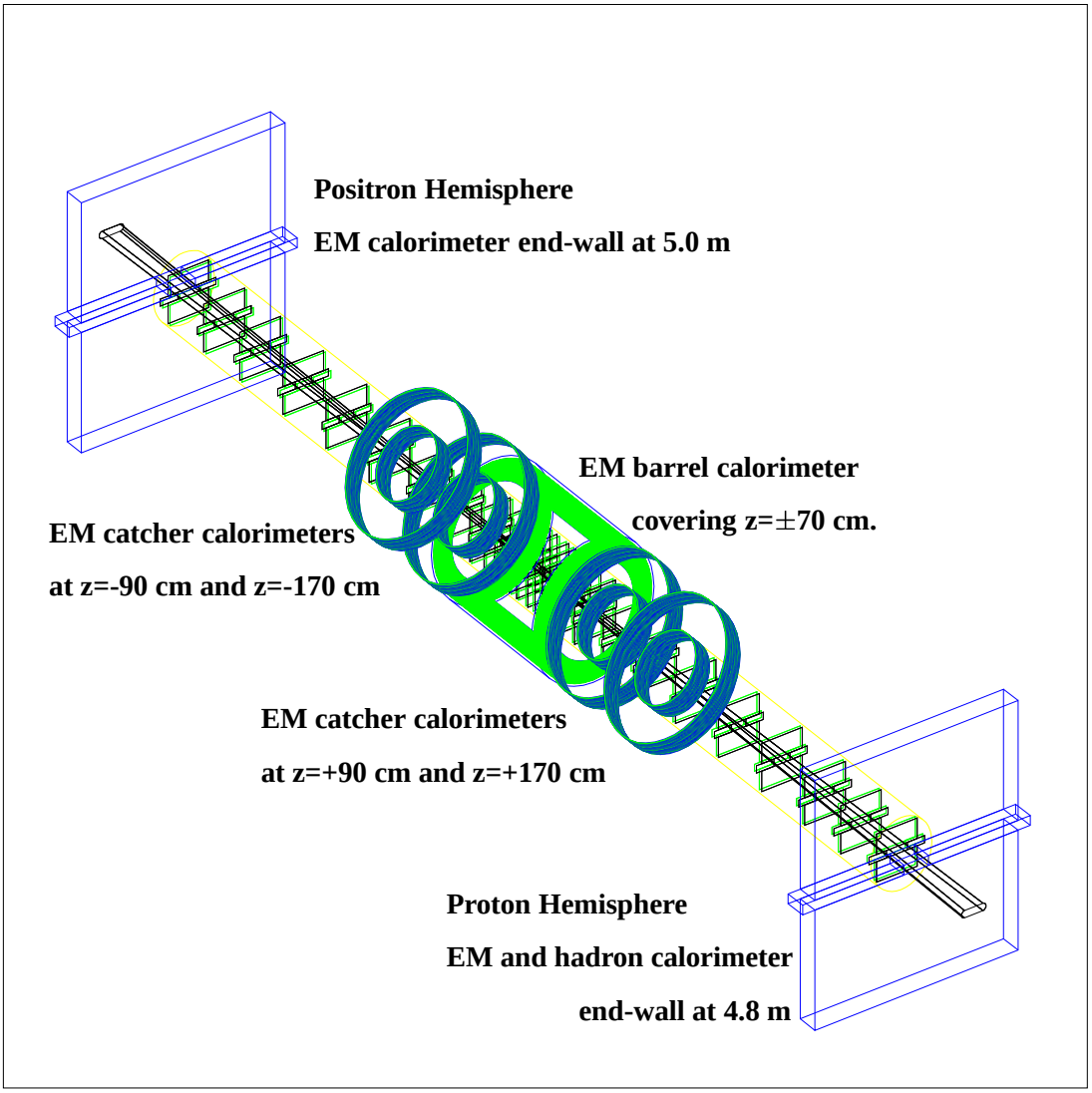

Figure 20: Schematic overview over the detector components within $\approx \pm 6$ m of the interaction point. The silicon planes are visible in the center. The calorimeter system consisting of a central barrel, 2 catcher rings on each side and end-walls is depicted in blue and green.

adjusted to the required cut-out. In order to leave space for the calorimetry the silicon planes extend to 4.9 m in the electron and 4.5 m in the proton hemisphere. Figure 19 gives an overview over the design.

Close to the interaction point the planes are relatively densely packed; they are used to track low momentum tracks with a large curvature and tracks with rapidities less than $\approx$1. Further out the planes have larger distances to enhance the lever arm for tracking particles with higher momenta.

3.1.4 Calorimetry

Over most of 4π only electromagnetic calorimetry is required. The goal of a compact detector leads to silicon-tungsten as the choice of technology. The active components are confined to a tube with a radius of 60 cm. In order to cover 4π in an elongated design as this, multiple structures have to be adapted. Figure 20 shows an overview over the full detector, Fig. 21 depicts the central region.

The central region in rapidity [$|\eta| < 1.3$] is covered by a barrel structure with an inner radius of 40 cm.

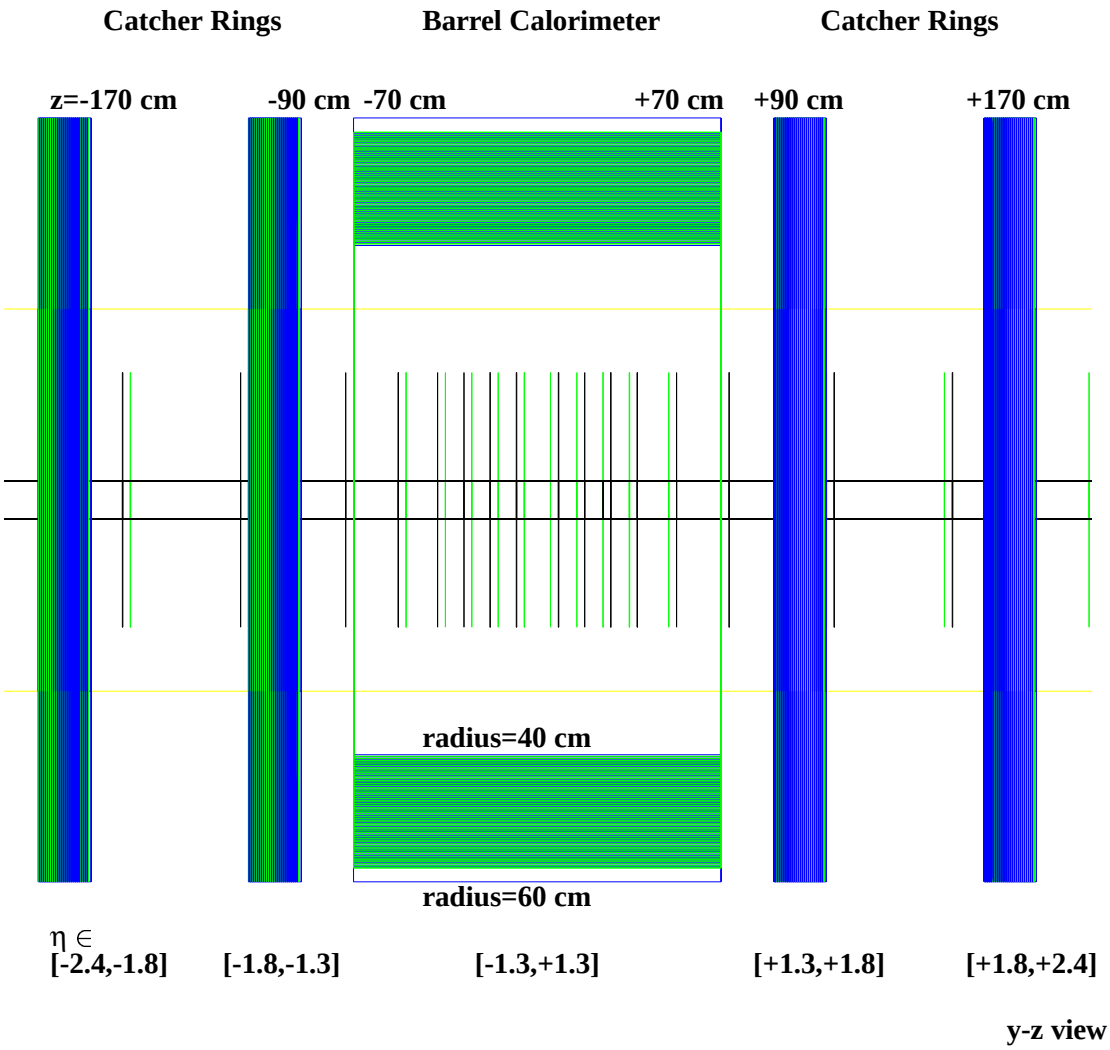

Figure 21: Overview over the central part of the em calorimeter system. The system is confined to a cylinder with a radius of 60 cm. Visible are the central barrel and the 4 catcher rings. Also visible are the active silicon planes[green] and support structures [black]

It extends to ± 70 cm in z. For a simple, non pointing layer geometry this results in a doubling of the path-length through a layer for a particle coming from the interaction point. The tungsten layers have a thickness of 1.75 mm which is equivalent to half a radiation length [X_0] per layer. For particles hitting the end of the barrel the effective layer thickness is 1 X_0. There are 50 layers resulting in an overall thickness of 25 X_0. The active medium are 500 μm thick silicon pads. The pad size will be around 1 cm$\times$1 cm and there will be three longitudinal sections. The segmentation will be discussed in the context of e-π separation.

High rapidities, $|\eta| > 2.4$, are covered by end-walls. These end-walls cannot be large enough to cover all the remaining rapidity range, because of the certainly limited aperture of the magnets. Therefore the intermediate range in rapidity is covered by “catcher rings”. Their absorber plates are perpendicular to the beam-line and cover radii from 30 cm to 60 cm. Two catchers are placed on each side of the interaction point. They start at z=$\pm$90 cm and z=$\pm$170 cm and cover the rapidity ranges from 1.3 to 1.8 and 1.8 to 2.4 with some reasonable additional overlap of about 10 % of a unit in rapidity.

Both catchers and the end-walls have tungsten absorber plates of 3.5 mm, i.e.1X_0, thickness. They have 25

layers and again silicon pads of 500 μm thickness as active elements. In addition there is a need for hadronic calorimetry in the proton hemisphere.

There are possibilities to use parts of existing calorimeters in this design. The requirements of the positron hemisphere end-wall could be met by the HERA-B tungsten shashlik calorimeter. The ZEUS uranium scintillator forward calorimeter with its electromagnetic and hadronic sections could be used as the proton hemisphere end-wall.

3.1.5 Proton remnant tagger

In order to measure precisely the cross sections for diffractive processes and exclusive reactions such as DVCS and vector meson production it is necessary to separate events in which the target proton remains intact from those where the proton dissociates into a higher mass hadronic states. The geometrical acceptance of the central detector for tagging the proton dissociation is only about 65 %. An additional hadron detector for tagging particles in the angular range from 1 to 8 mrad with respect to the proton beam direction and a neutral particle detector at zero (less than 0.5 mrad) angle are planned. The purpose of these detectors is to reach $\approx$ 100 % geometrical acceptance for tagging proton dissociation.

The forward hadron detector, FHD, will be located after the separation of the proton and electron beam-pipes about 25 meters away from the interaction point. It will surround the proton beam-pipe. The detector will consist of a high density hadron calorimeter, FHC, for energy measurement and two silicon strip counters, FHT, measuring multiplicities and both horizontal and vertical coordinates of the impact points of charged particles in front of the calorimeter. The measured energy and multiplicity will be used to distinguish between proton-dissociative and elastic reactions at large $|t|$. It is expected that for $-t > 1$ GeV^2, the elastically scattered proton will enter the detector. The measurement of the impact point of the scattered proton will help in the reconstruction of the variable t for DVCS and Vector Meson production with non-negligible values of Q^2 as well as in the correction for the energy leakage from the FHC for particles entering FHC close to its edge.

The neutral particle calorimeter (FNC) will be placed around 100 meters away from the interaction point where the zero angle neutral particles will leave the proton beam-pipe.

3.1.6 Photon calorimeter

A photon detector at zero angle with respect to the lepton beam direction is planned. It will cover about 1 mrad of the polar angle. The purpose of the detector is threefold:

- the bremsstrahlung photon measurement,
- the lepton beam diagnostic,
- tagging of the initial state radiation (ISR).

The luminosity measurement will be done by a measurement of the rate of bremsstrahlung events, $ep \to ep\gamma$. The cross section for this process is large and capable of giving large counting rate. The measurement can be done requesting a photon above some energy threshold [66] or a coincidence of the final state photon and the electron [67], or a single electron event. The electron will be measured in the central tracking detector.
The bremsstrahlung photons are emitted at small angles w.r.t. the lepton direction $< \Theta_\gamma > \approx \frac{m_e}{E_e} \approx 20\ \mu rad$ for the electron energy $E_e = 27.5$ GeV. The photon angular divergence is a convolution of the bremsstrahlung angular distribution with the electron beam divergence at the interaction point. We find that about 98% of the bremsstrahlung photons are contained in the polar angle interval of 0.54 mrad for a typical angular divergence of the beam of 0.2 mrad in the horizontal plane.
The photon will be detected in an electromagnetic calorimeter about 100 meters away from the interaction region. In addition to the energy also its impact point will be measured in order to monitor the beam conditions at the interaction point.
Due to the proposed design of the interaction region including dipole fields, the photon detector will be exposed to synchrotron radiation with a power of about 1800 W for an electron beam current of 60 mA. This radiation

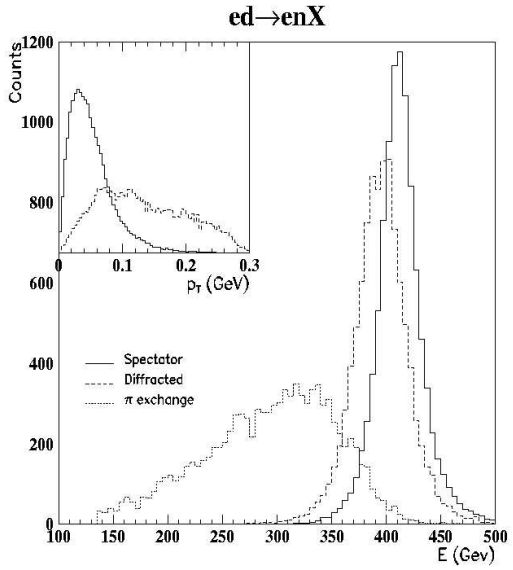

Figure 22: Leading neutron energy spectra for various processes [70].

has a critical energy of 150 keV. Therefore the calorimeter has to be radiation hard and shielded by a filter. On one hand the filter has to absorb intense synchrotron radiation and on the other the degradation of the calorimeter's energy resolution and linearity introduced by the filter should be minimal. The filter material should have low Z and a thickness of 2–3 radiation lengths. A possible solution for the calorimeter would be a Cerenkov sampling calorimeter [68] in which the tungsten radiator plates are interleaved with quartz-fibers acting as active medium. The fibers are read out with photomultipliers. Synthetic fused silica fibers are known for their radiation resistance. The quartz-fiber calorimetry has proven suitable in high-radiation environment [69]. For a calorimeter with a 0.36 sampling fraction an energy resolution of $19\%\sqrt{E(GeV)}$ can be obtained [68]. Moreover alternating directions (horizontal and vertical) of the fibers in adjacent planes can form a position detector for the photon impact point measurement. The depth of 25 radiation lengths will ensure good shower confinement.

3.1.7 Spectator tagging

As discussed in Sec. 2.4, in *ed* scattering it is important to identify the spectator nucleon which does not participate in the *eN* reaction. Such spectators carry approximately half of the deuteron energy. Due to the Fermi motion of the nucleons bound within the deuteron, their energies are smeared with an R.M.S of $\approx 3\%$. For the case of a hard *eN* scattering an energy measurement with resolution of a few per cent is adequate to identify the spectator nucleon with reasonable purity. This is shown in Fig. 22 for neutrons produced via π exchange. However, when the *eN* scattering is an elastic diffractive process, the final state nucleons have an energy spectrum similar to that of the the spectators, also shown in Fig. 22. The energy measurement alone cannot identify the spectator in this case.

The spectator nucleons have an inherent p_T due to their Fermi motion with an R.M.S of ≈ 30 MeV/c as shown in Fig. 23. Also shown is the p_T distribution for elastic diffractive nucleons. A good separation of the two processes is possible with a p_T measurement. In addition to the Fermi motion, the spectator nucleons also have transverse momentum due to the deuteron beam divergence. For HERA I optics this had an R.M.S in the range 25-50 MeV/c. Thus the effective p_T distribution of spectators has an R.M.S in the range 40-60 MeV/c. A p_T measurement with resolution less than this value will provide the best possible identification of spectator nucleons.

A possible spectator tagging system for a HERA I type of beam line is shown in Fig. 24. Near 70 m from the interaction point the beam is bent vertically by ≈ 6 mrad. Approximately 100 m from the interaction point a calorimeter is placed below the beam pipe along the zero degree line to detect undeflected neutrons. A similar

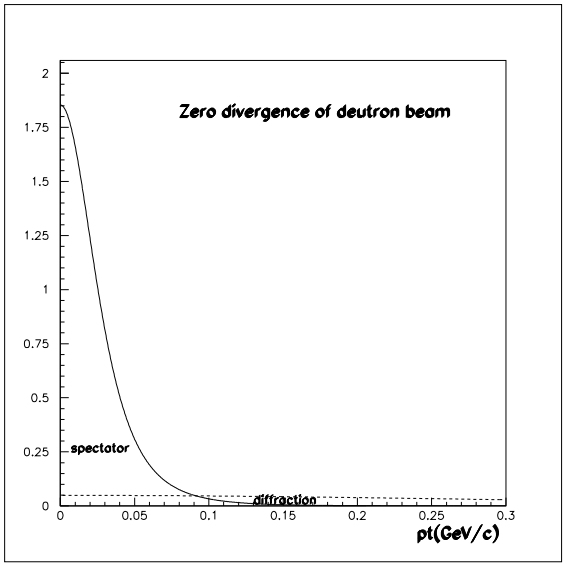

Figure 23: p_T distributions of spectator and elastic diffractive nucleons [65].

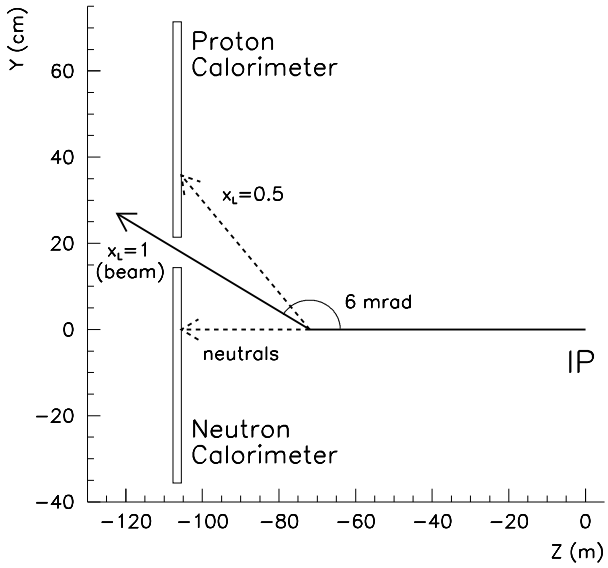

Figure 24: Spectator tagging system in the deuteron beam direction downstream of the interaction point.

calorimeter is placed above the beam pipe to detect protons with $x_L = E_p/E_d$ small enough to be bent out of the beam pipe. The calorimeters are similar to the H1 and ZEUS forward neutron calorimeters, which have achieved an energy resolution of $\sigma_E/E = 65\%/\sqrt{E}$ and a position resolution of $\sigma_x = 2.5$ mm [71]. The energy resolution at 460 GeV is 3%, sufficient to resolve the spectator peak. For neutrons the p_T resolution is $\sigma_{p_T} = 11\,\mathrm{MeV/c} \oplus 0.03 p_T$, much smaller than the R.M.S. of the effective p_T distribution of spectators. To estimate the p_T resolution for spectator protons a simulation of the HERA I beam-line was used. Figure 25 shows the x-position versus p_x for protons with $p_y = 0$ for several energies near $x_L = 0.5$. The slope of the lines gives the contribution to the p_T resolution due the the position measurement, which is in the range σ_{p_T} = 4-8 MeV/c. The spacing of the lines gives the contribution to the p_T resolution due to the energy measurement, which is in the range σ_{p_T} = 15-30 MeV/c. Overall the p_T resolution is typically $\sigma_{p_T} \leq 30$ MeV/c, smaller than the R.M.S of the effective p_T distribution of spectators. Thus such a tagging system will provide the best possible identification of spectator nucleons allowed by the inherent Fermi motion and beam divergence.

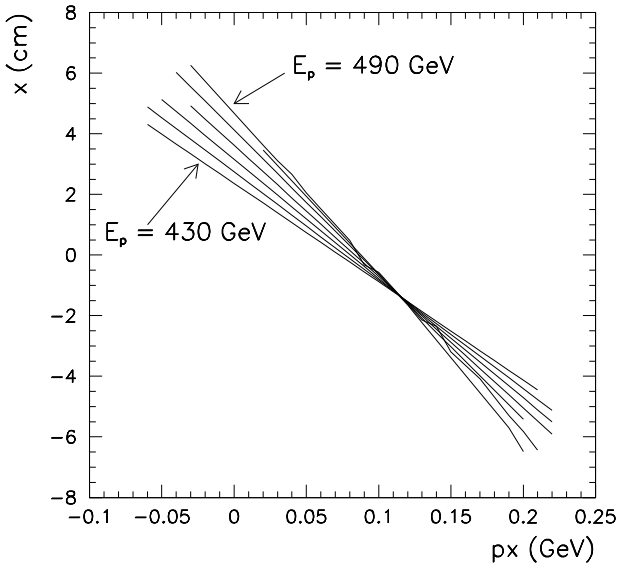

Figure 25: Proton x-position at the tagging calorimeter versus p_x for protons with $p_y = 0$ and energies in the range 430-490 GeV.

3.2 Detector performance

The detector performance was studied using a full GEANT3 simulation of the detector as described in the previous section. Interactive GEANT was used embedded in "atlsim" [74], a tool developed for ATLAS [2].

3.2.1 Acceptance

The acceptance of the tracking system was studied using positrons "injected" into the detector at the origin with negative rapidity. A flat phase-space in energy, rapidity η and azimuth angle ϕ was used. A minimum of three space-points is needed to reconstruct a track. However, it is desirable to have redundancy and at least 4 hits per track. Figure 26 depicts the acceptance for three required hits binned in η and ϕ for several energy bins. The ϕ dependence of the acceptance is purely geometrical due to the field configuration and the oval shaped beam-pipe. In the simulation the beam-pipe is symmetric in x which will not be the case in the end. So we expect to gain acceptance on one side due to a beam-pipe not opening on the proton side. However, we will lose acceptance again due to pumps integrated into the pipe. We can choose the side on which the pumps will be installed and will have to study where the small effect expected is least affecting physics. The acceptance in the +z direction (proton hemisphere) is about the same as in the -z direction.

Up to an energy of about 8 GeV the acceptance extends to rapidity -8. For large energies at large rapidities the magnetic field is not able to separate the positrons sufficiently to be seen in the tracking planes. The tracking system is not designed to independently measure tracks with rapidities less than $\approx$1. However, we have 100 %($\approx$50 %) efficiency for two hits for $|\eta| \in [1.,.75]$([.75,.5]) over the full energy range. This information can be combined with calorimeter information which is best in this region. We do not pursue this further at this stage.

The acceptance in the physics variables W and Q^2 is shown in Fig. 27 for the requirement of at least three or 4 hits. We have good acceptance down to Q^2 of 0.1 GeV^2 over the complete W range. This is the main focus of this detector design.

[2] Special thanks to Denis Salihagic and Pavel Nevski for their help setting up the simulation.

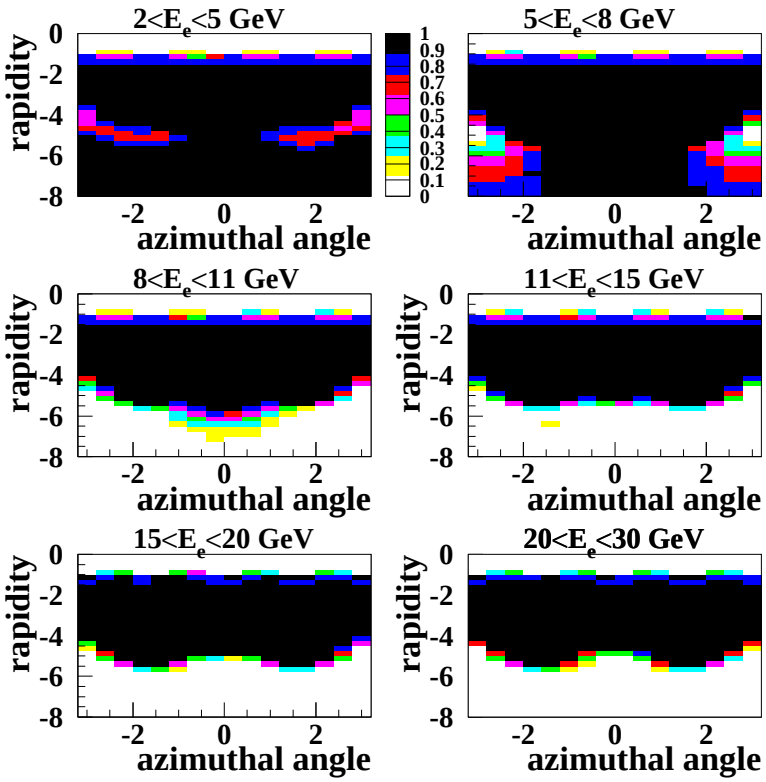

Figure 26: Acceptance of the tracking system in different energy bins vs. azimuth angle and rapidity. A track is counted as accepted if there are at least three hits in the tracking system.

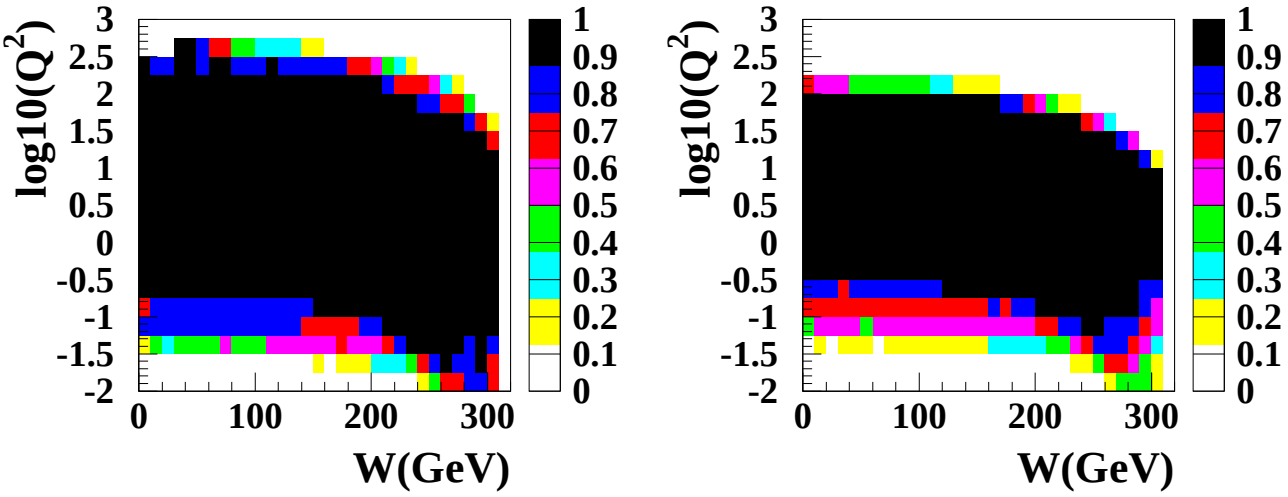

Figure 27: Acceptance of the tracking system vs. W and Q^2 assuming E_p=920 GeV. For the left plot a track is counted as accepted if there are at least three hits. For the right plot 4 hits were required.

3.2.2 Momentum Resolution

The momentum resolution was studied using different assumptions about the material in the detector, as shown in Table 1. These assumptions do not correspond to real technical designs; they are merely used to study the influence of material to guide later designs. For each scenario 10 million positron tracks were simulated. A

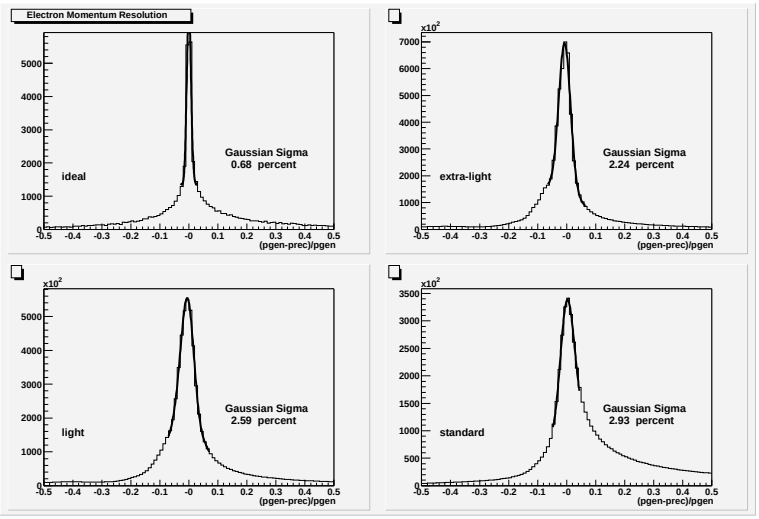

Figure 28: Distribution of the normalized difference between generated and reconstructed momentum for an ideal detector, top left, the extra-light, top right, the light, bottom left, and the standard, bottom right, scenario [see also Table 1].

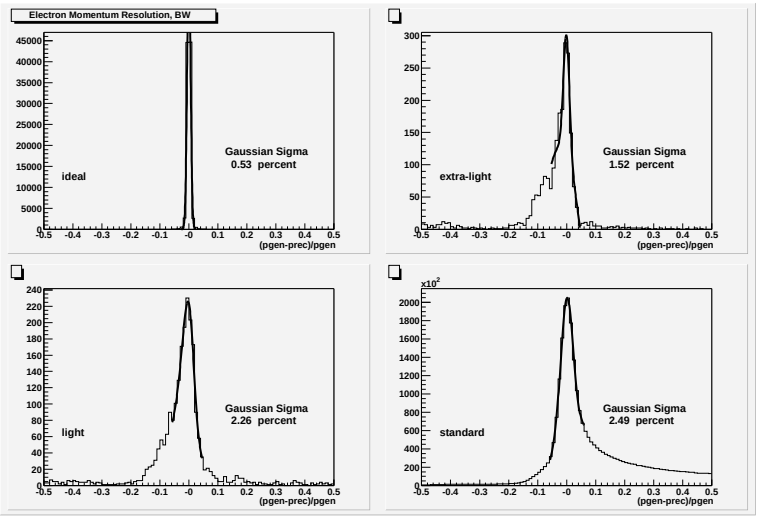

Figure 29: As in fig 28, but restricted to tracks with $\eta > 3.1$.

phase-space flat in energy, rapidity η and azimuth angle ϕ was chosen. It covers an energy range of 2 GeV to 30 GeV, a rapidity range of -0.1 to -6. and 2π in ϕ. All hits caused by the primary particle as well as those from secondary processes were handed to a reconstruction program.

The reconstruction program uses a fit program provided by V.Blobel. The components perpendicular and parallel to the magnetic field are treated separately and are then recombined. Two physics processes directly influence the resolution. One is multiple scattering, the other one Bremsstrahlung. While multiple scattering changes the track in a random way, Bremsstrahlung always causes an energy loss and thus a bias. Some Bremsstrahlung photons convert and cause extra hits. In addition, some of the primary positrons interact and create a shower. All these effects make some pattern recognition, even for a preliminary study, indispensable. Normally a hit resolution σ_h of 20 μm is assumed. After a first fit using all points, the point with the largest residual is taken out if it has a residual larger than 3 σ_h. This procedure is continued until either all points have a residual of less than 3 σ_h or there are only 3 points left. A track is removed from the sample if the average

Table 1: Material budgets used to study the momentum resolution. 600 μm silicon represent 2 silicon wafers, 1.2 mm CF assume a uniform support structure of 1.2 mm carbon fiber and the beam-pipe is assume to have a thickness of 500μ m aluminium.

Scenario	silicon	support	beam-pipe
standard	600 μm	1.2 mm CF	500μ m Al
light	600 μm	1.2 mm CF	none
extra-light	600 μm	none	none

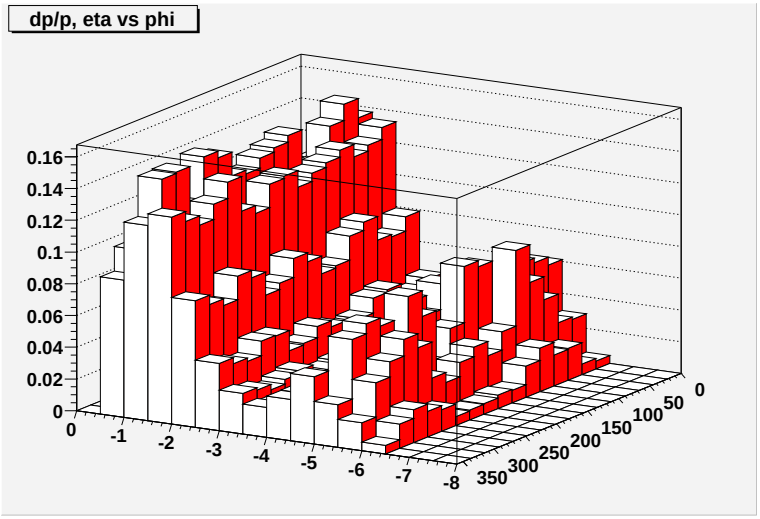

Figure 30: δp/p vs ϕ and η integrated over all momenta for the standard material budget and 20 μm hit resolution.

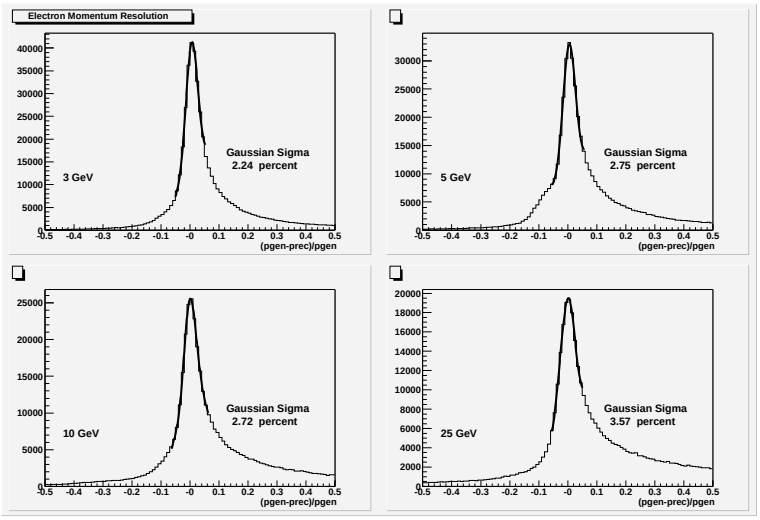

Figure 31: δp/p for 4 different momentum bins.

residual is larger then 2 σ_h. This affects approximately 4 % of the tracks.

In Fig. 28 the overall distribution of the normalized difference between reconstructed and generated momentum is shown for the scenarios from Table 1 and for an ideal detector with no material. Obviously the

Table 2: δp/p for different parts of phase-space for different material budget scenarios. A hit resolution of 20 μm is assumed

.

Scenario	standard	light	extra-light	ideal
full phase-space	2.5%	2.3%	2.0%	0.7%
$\eta > 3.1$	2.1%	2.1%	1.4%	0.6%

Table 3: δp/p for $\eta > 3.1$ in dependence of hit resolution and material budget.

Hit resolution	20 μm	40 μm	60 μm	80 μm	100 μm
standard	2.5%	2.6%	2.8%	3.3%	3.4%
light	2.3%	2.4%	2.9%	2.8%	3.2%

material is important for the central part of the distribution which is dominated by multiple scattering. However, it is even more important for the tails, especially the one on the right side caused by energy loss due to Bremsstrahlung. This tail contains up to 20 % of the tracks. Figure 29 provides the same distributions as Fig. 28, but restricted to very forward tracks with $\eta > 3.1$, i.e. $\theta > 175^o$. The distributions are fit with a function

$$ae^{-\frac{x-<x>}{2\sigma^2}} \cdot e^{b(x-<x>)^3} + (a_p + b_p x + c_p x^2)$$

The central Gaussian part is represented by σ which is quoted as the resolution δp/p. In Table 2 values are given for the different scenarios also used in Figs. 28 and 29.

The influence of the hit resolution σ_h was also studied. Table 3 lists the influence of σ_h on δp/p for the standard and light material budget in the forward phase-space region previously used. The hit resolution is obviously not critical below at least 50 μm when reasonable amounts of material for a silicon tracker are assumed. This is understandable, as hits in tracking stations with 1 % X_0 and a lever arm of about 50 cm, as is the situation for forward tracks in the current design, are subject to distortions of about 70 μm from multiple scattering alone. However, hit resolutions become more important, if the the material can be reduced. This limits the choice of alternative technologies. For all further studies a σ_h of 20 μm, which is easily achievable with silicon, is assumed.

Due to the field configuration the momentum resolution depends on the angle φ and the rapidity η. This is demonstrated in Fig. 30. Due to the detector design the resolution is, however, basically independent of the momentum itself for any given η and φ. In Fig. 31 the resolution is given for 4 different energies integrated over η and φ.

The momentum resolution for pions is expected to be better than for positrons, as they have less probability to undergo Bremsstrahlung. This mainly affects the tails of the δp/p distribution which should be substantially smaller. The relevant study is in progress.

3.2.3 Energy Resolution

The energy resolution was studied generating positrons at the origin, tracking them through the magnetic field and studying the response as seen in a full GEANT generation. No segmentation was simulated and no energy threshhold corresponding to read-out electronics was taken into account. The results is shown in Fig. 32.

In the barrel the energy resolution depends on the rapidity of the particle, i.e. on the impact angle. In Fig. 32 results are given for the center and the end of the barrel where the effective plate-thickness doubles. The curves shown correspond to

$$14\%\sqrt{E} \oplus 2\% \qquad \text{and} \qquad 15\%\sqrt{E} \oplus 2\%$$

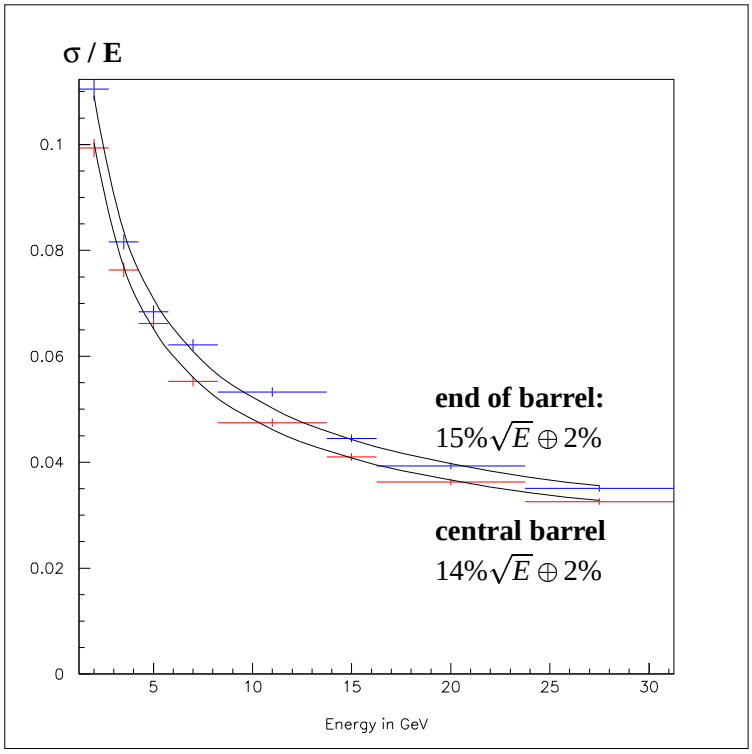

Figure 32: Energy resolution of the silicon tungsten calorimeter for scattered positrons hitting the center [red markers] or end [blue markers] of the barrel.

for the central and end part of the barrel respectively. Here no correction was applied to adjust the calibration to the change in sampling fraction. The situation in the catcher rings and end-wall[s] is similar to that at the end of the barrel, as the plate-thickness was chosen to also correspond to $1X_0$ there.

The calorimeter is not used to determine the energy of hadrons over most of 4π. Hadronic calorimetry is only foreseen for the proton hemisphere end-wall. The ZEUS forward calorimeter would meet the specification of an energy resolution of around 50 % $\sqrt{E}$.

3.2.4 e-π Separation

The barrel calorimeter was used for the studies presented here. As a first step the energy response was studied. For positrons the simulation confirms an energy independent response over the range of 2 GeV to 30 GeV. The calibration constant needed to adjust the visible energy to the generated energy changes by 3.3 % over the length of the barrel calorimeter. This was corrected for in all studies presented.

The calibrated visible energy in the central part of the barrel calorimeter for positrons and positive pions is depicted in Fig. 33 for various energies. The energy response for the pions clearly shows the peak at very low energies associated with non interacting pions. For higher energies the showers are not contained and thus the visible energy for interacting pions is also lower.

Assuming knowledge of the particle momenta from the tracker an e-π-separation solely based on the energy response is possible. Figure 34 shows the result for a cut on 90 % of the visible energy compared to the known momentum for the central and the end part of the barrel. The separation is significantly worse for the end part. At low energies this is caused by the cruder sampling due to the geometry. At high energies the result just reflects the fact that the pion showers are better contained in the end part due to the larger effective depth . However, the results from this simple approach show that an efficient and powerful e-π separation is rather easy at energies above 5 GeV. Therefore the focus of further studies are the low energies.

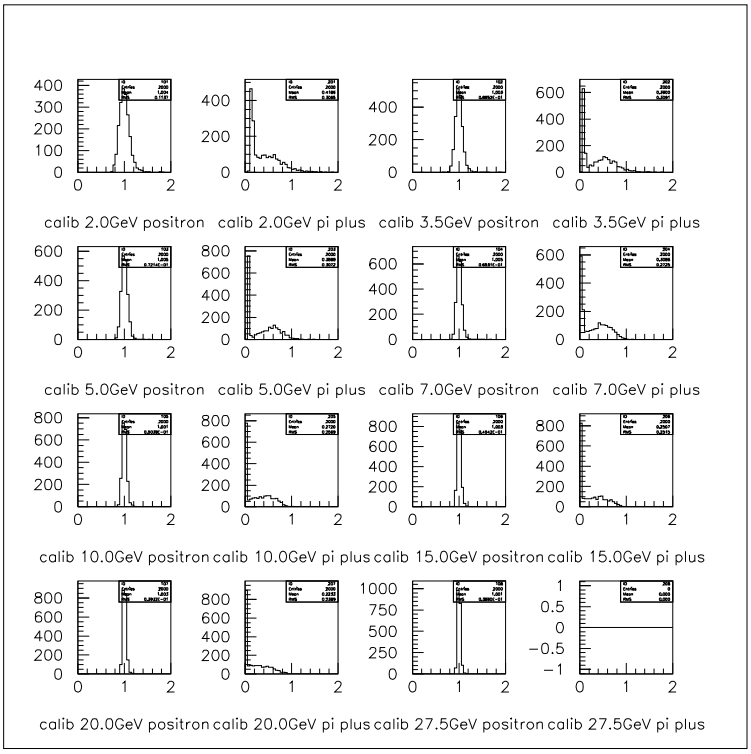

Figure 33: Normalized visible energy in the central part of the barrel calorimeter for positrons and pions of various energies. The normalized visible energy was calibrated to be 1 for electrons. The highest energy for pions was not simulated.

Electromagnetic and hadronic showers are different in longitudinal and in transverse development. Both aspects were studied.

The barrel calorimeter has 50 layers and we assume three longitudinal segments. The optimization of the longitudinal segments was done for the 2 GeV showers, as they are the most difficult case. The segment borders were chosen to correspond to 50 % and 150 % of the depth of the shower maximum. The resulting segmentation changes with z along the barrel to optimize e-π-separation everywhere.

Cuts on the ratios of the longitudinal segment energies E_1, E_2 and E_3 were used in addition to a varying overall cut on the ratio of visible, E_{vis}, and true energy, E_{true} . For the longitudinal segments we used the following cuts

$$\frac{E_1}{E_2} < 1.0 \qquad \text{and} \qquad \frac{E_3}{E_2} < 4.0$$

to identify electrons. The cut on E_{vis}/E_{true} started at 0.75, yielding the maximum electron finding efficiency, and was subsequently increased. However, we also determined the e-π separation without such a cut. In that case we identify events with $E_{vis} < 1$ GeV as non-interacting pions. This is justified, because we do not attempt to identify particles with an energy of less then 2 GeV at this point. Figure 35 shows the results for the central and the end part of the barrel. A rejection power of 20 is reached with very high efficiencies.

A complementary study focusing entirely on the transverse size of the showers also yields rejection factors larger than 20 for efficiencies above 95 %. This study was also used to optimize the cell size of the calorimeter. A segmentation of 1 cm × 1 cm, i.e. close to the Moliere radius, was found to be optimal for the central part of the barrel. For the moment we assume a non-pointing geometry with this cell size over the whole barrel.

The development of the transverse size of the shower in the three longitudinal sections was also studied. Cuts were developed for the overall transverse size T, the transverse sizes in the segments T_1, T_2 and T_3 and their ratios. In addition the total number of three dimensional cells hit N_{cell} was considered. The cuts to identify

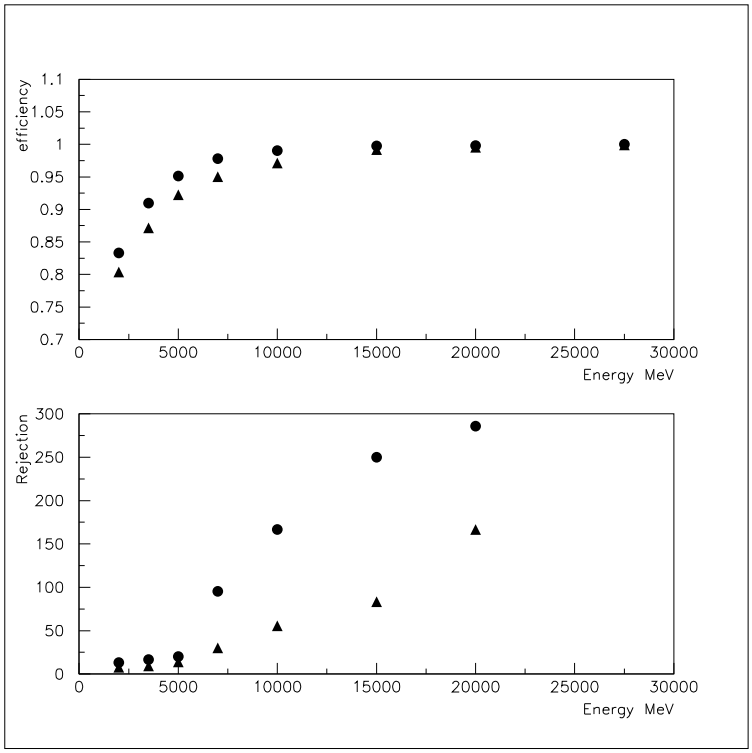

Figure 34: Efficiency [top] and rejection power [bottom] of a 90 % cut in visible energy for known momenta. The dots correspond to the central part, the triangles to the end part of the barrel calorimeter.

Table 4: Cuts on the transverse size development of the showers used for e-π separation. For variable descriptions see text.

Variable	$T <$	$T_2 <$	$T_3 <$	$T_2/T_1 <$	$T_3/T_2 <$	$N_{cell} >$
$\eta = 0$	10 cm	10 cm	10 cm	20	10	25
$\eta = 1$	12 cm	15 cm	15 cm	25	20	25

an electron are summarized in Table 4. Figure 36 depicts the results when these cuts are combined with the cuts used in Fig. 35.

It should be noted that for 2 GeV showers a rejection factor of larger than 20 is achieved even if no knowledge about the true energy is assumed. This is especially important for the central part of the calorimeter. A rejection factor larger than 50 with efficiencies above 90 % are reached over the length of the barrel, if a momentum measurement is assumed. All cuts presented here for e-π separation were optimized for 2 GeV showers. Therefor the rejection achieved for 3.5 GeV, especially for $\eta = 1$, is worse. However, as the number of pions to discriminate against becomes smaller with energy, this does not seem a problem at the moment.

More design optimization for the various parts of the calorimeter is needed. In this context also a neural network analysis using full cell information is planned. Another technical option is to choose a digital instead of an analogue readout. This would allow for very fine longitudinal and transverse segmentation. The small three dimensional cells would reveal the shower structure. The number of holes within the shower volume would be one of the observables to separate hadronic and electromagnetic showers.

The barrel calorimeter could also have a number of layers varying with z. The effective depth would always be kept at 25 X_0. The 25 inner layers would extend to ± 70 cm and the 25 outer layers would gradually be reduced in length to $\approx \pm 20$ cm. This would reflect the change in longitudinal segmentation described earlier

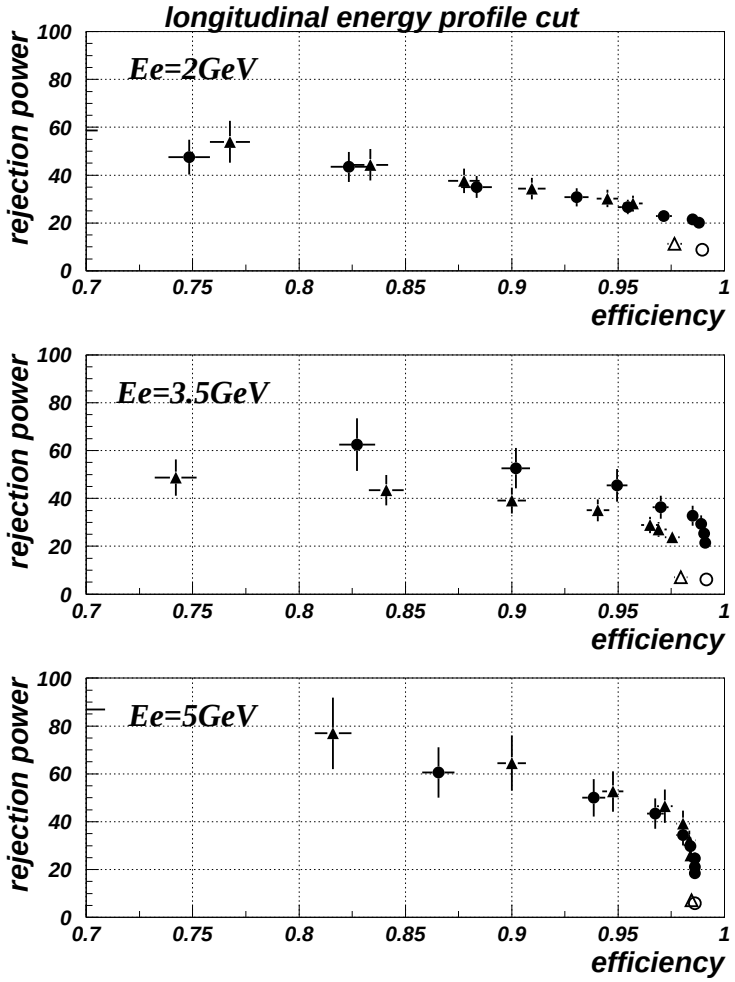

Figure 35: Rejection power vs efficiency for varying overall energy cuts plus longitudinal segment cuts. Results are given for the central (dots) and end (triangles) part of the barrel calorimeter for energies of 2 GeV, 3.5 GeV and 5 GeV. The open symbols indicate results using no cut on the ratio of the visible and true energy; however, showers with less than 1 GeV energy deposition are considered to be non-interacting pions and are not considered.

and not degrade the overall performance. However, it would safe a substantial amount of silicon and tungsten and the placement of read-out electronics and support mechanics would become easier.

Clearly more studies are needed to optimize e-π separation in all parts of the calorimeter. However, it seems well feasible to meet the requirements to find and identify positrons down to an energy of 2 GeV. At 95 % efficiency to identify a positron we can conservatively assume a rejection factor of 20 for pions. In the presence of a 2 GeV positron we expect a maximum of three positively charged pions with a larger energy in the positron hemisphere. Applying an algorithm that tests the particles ordered by energy we get a probability of 85 % to not misidentify any of the pions as a positron. At 90 % positron identification efficiency we can, again conservatively, assume a rejection factor of 30. This yields a 90 % probability to not misidentify a pion and thus an 80 % probability to find and identify the wanted positron in this worst case scenario.

3.2.5 Proton dissociation tagging

So far we have not chosen a particular design for FHD and FNC detectors, since they have to be fully integrated with an unknown realization of the HERA beam-line. In this sense the following considerations should be taken

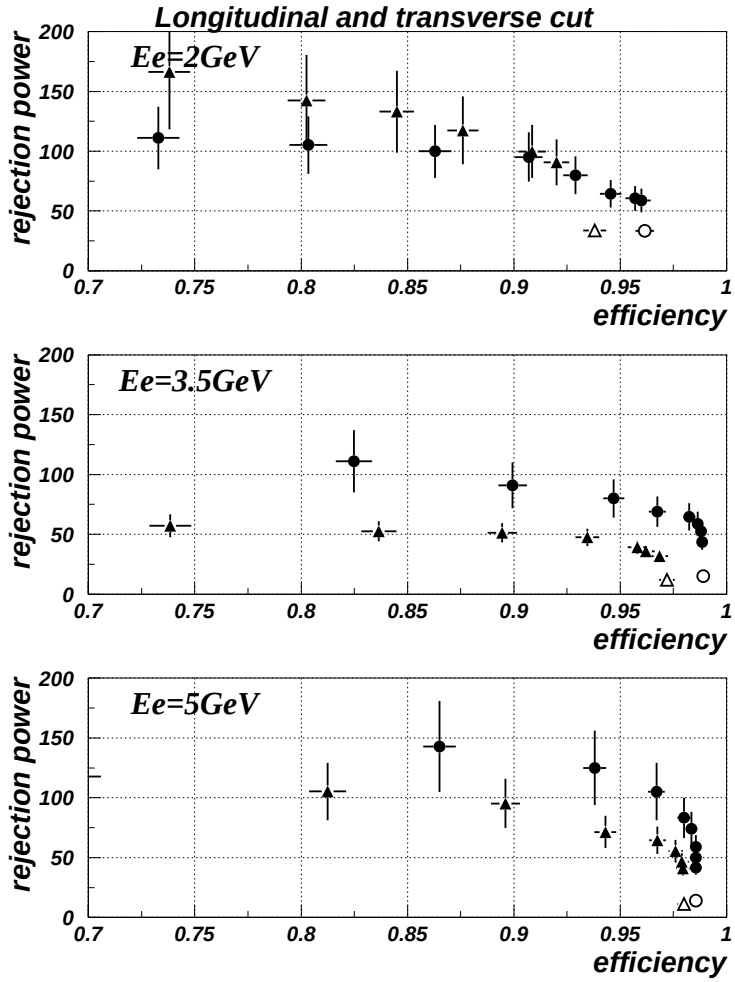

Figure 36: Rejection power vs efficiency for varying overall energy cuts plus longitudinal and transverse segment cuts. Results are given for the central (dots) and end (triangles) part of the barrel calorimeter for energies of 2 GeV, 3.5 GeV and 5 GeV. The open symbols indicate results using no cut on the ratio of the visible and true energy; however, showers with less than 1 GeV energy deposition are considered to be non-interacting pions and are not considered.

as a proof of principle rather than a real design.

In a simulation, the FHD surrounds a 5 cm×5 cm beam-pipe at $z = 25$ meters and is of rectangular shape 25 cm×25 cm. The FNC covers 0.5 mrad of the polar angle around proton beam direction. In Fig. 37 the proton remnant tagging acceptance for central detector, FHD and FNC as well as the overall acceptance are shown as a function of a mass of the proton-dissociative state, M, and as a function of $-t$. The tag was defined as a minimum energy deposition of 1, 10 and 100 GeV in the central detector, FHD and FNC respectively. The overall acceptance is almost M and t independent and about 100 %.

Almost 100 % efficiency for tagging proton dissociation allows a very good separation of the elastic and proton-dissociative processes at $-t < 1$ GeV^2 where the elastically scattered proton escapes the beam-pipe undetected. At $-t > 1$ GeV^2 the separation will be based on the energy and particle multiplicity measured in FHD. In addition the measurement of the x and y coordinates of the proton at $z = 25$ meters will help in the reconstruction of t. The measurement will be influenced by the positions and magnetic fields of HERA beam-line elements. The latter can be aligned using samples of vector mesons produced with $Q^2 \approx 0$ where the variable t is precisely measured from vector meson decay products only.

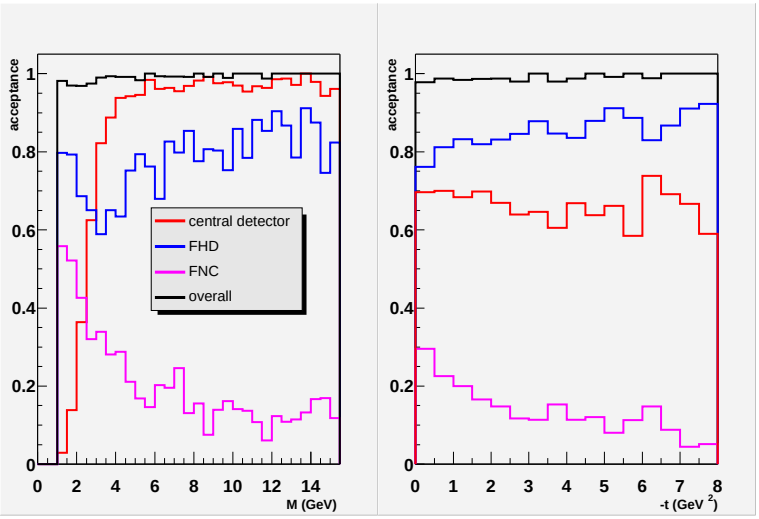

Figure 37: Proton remnant tagging acceptance for central detector, FHD and FNC as well as the overall acceptance as a function of M and $-t$.

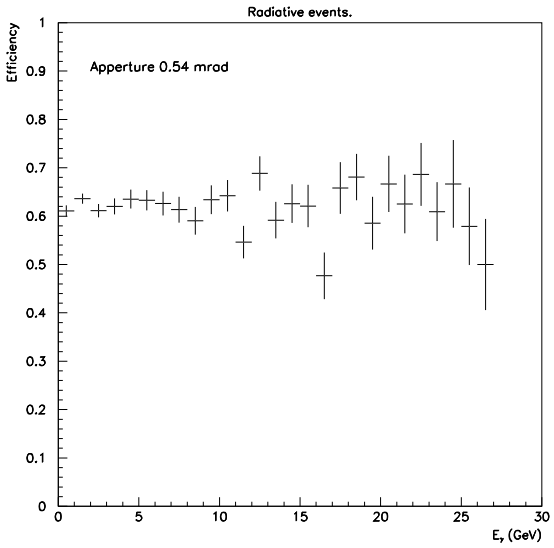

Figure 38: The acceptance of the ISR photons in 0.54 mrad polar angle interval as a function of the photon energy E_γ. The photon direction is smeared with a typical angular divergence of the electron beam.

3.2.6 Initial state radiation measurements

The photon detector can be used to tag the initial state radiation (ISR) photons in deep inelastic scattering. The emission of hard radiation in the initial state leads to a change of the event kinematics lowering $\sqrt{s}$. Hence, smaller Q^2 and higher x values can be accessed. Such events can be used to measure the longitudinal structure function F_L [72, 73]. On the other hand anti-tagging these events will allow the minimization of the ISR effects on other measurements.

The angular distribution of ISR photons is broader than that for the bremsstrahlung ones.This leads to lower acceptance. In Fig. 38 the acceptance of the ISR photons in the polar angle aperture of 0.54 mrad is shown as a function of the photon energy. The photon direction was smeared with a typical angular divergence of the

lepton beam. The acceptance is energy independent and about 60%. This will allow a selection of the event sample with hard initial state radiation and the measurement of F_L and F_2 at different $\sqrt{s}$. The presence of the filter in front of the photon detector will disturb the energy measurement. Part of the photons will interact in the filter. This will lead to a partial absorption of the photon energy in the filter hence smaller measured energy in the calorimeter. This effect will decrease with increasing photon energy.

3.2.7 Background rejection

There will be several types of backgrounds to deal with in the detector design discussed here:

- Beam related background, such as synchrotron radiation, off-momentum electrons and secondaries from upstream proton interactions. We do not expect these events to be mistaken for real events, as they can easily be removed with timing and vertex constraints. However, if the rate is too high, overlay or even radiation damage problems could occur. A detailed study of these backgrounds has not yet been performed, but would clearly be an important issue in future studies of this type of detector design.

- Background from Bethe-Heitler overlays. There will be a high rate of electrons in the detector from the $ep \to ep\gamma$ Bethe-Heitler reaction. The expected rate approaches 100 kHz for a luminosity of $1 \cdot 10^{31}$ cm^{-2} s^{-1}. These extra electrons will need to be properly treated in the analysis procedure. We note that this reaction also allows a luminosity measurement with the main detector.

- Photoproduction events mistakenly reconstructed as DIS events. This type of background is expected to be less severe than in HERA-I, since, at large W, the scattered electron will be visible in the main detector for all Q^2 values down to Q^2_{min}. For smaller W, the visible $E - Pz$ in the detector will be small, and the events will be rejected easily. We have studied the expected $E - Pz$ resolution from our detector design as follows:

  – charged particles in the detector acceptance were smeared with the expected momentum resolution.
  – electrons and photons were smeared with the expected calorimeter resolution.
  – neutrons and K^0_L were assumed not to be measured.

  The expected resolution in $E - Pz$ is given in Fig. 39, and it is seen that a resolution of about 1.5 GeV is expected. This is largely sufficient to reject photoproduction events at low W.

- Events with initial state photon radiation. These events can be controlled both by measuring the radiated photon (see previous section), or by measuring $E - Pz$ in the central detector. As discussed above, the $E - Pz$ resolution is expected to be about 1.5 GeV, and this will provide a valuable tool for measuring or rejecting events with substantial initial state radiation.

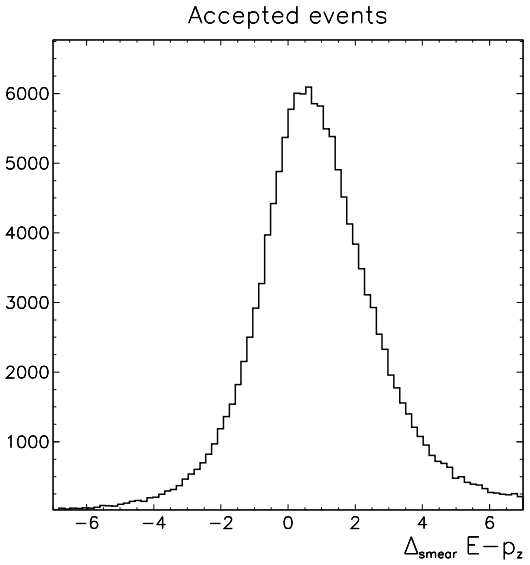

Figure 39: The distribution of $(E-Pz)_{true} - (E-Pz)_{meas}$ expected for reconstructed events.

3.3 Physics performance

In this section, we give a few results from our simulation studies for the physics processes which are considered as the highlights of the program.

3.3.1 Structure function measurements

The acceptance for the scattered electron has already been shown in Fig. 27. As can be seen in the figure, the scattered electron is measured over the full W (or x) range for $0.3 < Q^2 < 50$ GeV^2. Using the electron method to reconstruct event kinematics yields a few % Q^2 resolution over most of the kinematic range. The x resolution is given by

$$\frac{\delta x}{x} = \frac{1}{y}\frac{\delta p}{p} \oplus 2\frac{\delta \varepsilon}{\varepsilon}$$

where p, ε are the scattered electron momentum and angle, respectively. At the smallest values of x, the electron energy is small and the kinematic quantities will be measured with high precision. However, as x increases, y decreases (for a fixed Q^2) and the electron method rapidly loses resolution in the measurement of x (or W). The kinematic range which can be used with the electron method assuming a momentum resolution of 1 % is shown in Fig 40. This resolution is not achieved with the standard detector design considered above. Reaching this goal will either require a tracking system with considerably less material, or a higher precision calorimeter ($\sigma_E \leq 5\,\%\sqrt{E}$).

For high-x events, the kinematic variables can be determined precisely from the electron (to fix Q^2) and the forward jet (to give x). The kinematic coverage using this mixed method is also shown in Fig 40. An expanded view of the high-x coverage, along with expected cross sections calculated with the ALLM parametrization [75], is shown in Fig. 41. The large rapidity coverage of this detector yields full jet acceptance at high-x already for moderate Q^2 values, particular for the lower energy proton running, thus greatly increasing the visible cross section for these events in comparison to the existing H1 and ZEUS detectors. We note that the scattered electrons are seen in the detector up to $x = 1$, such that an integrated measurement of the cross section is possible beyond the limit where jets can be used to measure x. This will allow the measurement of the integral of F_2 from the edge of the phase space coverage shown in Fig. 41 to $x = 1$.

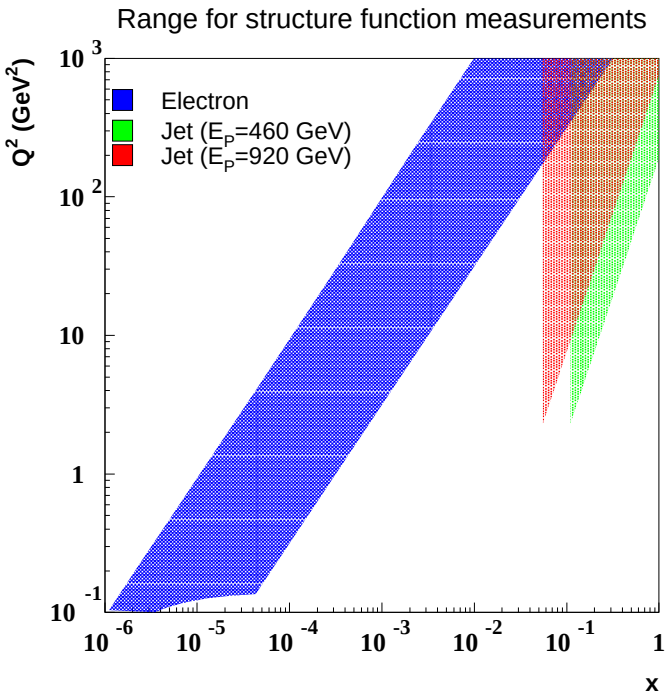

Figure 40: The kinematic coverage with the electron method assuming a 1 % electron momentum measurement at small-y (blue shaded area) and with a combination of the electron and jet information (red shaded area, $E_P = 920$ GeV, green shaded area $E_P = 460$ GeV). The intermediate region requires a measurement of y from the hadronic system.

For intermediate x values, where neither the electron nor electron+jet methods work, other techniques such as the double angle method must be employed. We have not yet studied the performance of such techniques with this detector design, but it is expected that these methods will substantially increase the range shown in Fig. 40. As a first indication of the performance of this detector design, we have looked at the y reconstruction using the hadronic system. In this method, y is calculated as

$$y_{JB} = \frac{\sum_i (E_i - P_{Z,i})}{2E_e}$$

where the sum runs over all particles excluding the scattered electron, and $E_i, P_{Z,i}$ are the energy and z-component of the momentum of the particle, respectively. E_e is the electron beam energy. A minimum energy of 100 MeV was required for the calorimeter energy deposits or track momenta. The reconstructed y_{JB} is compared to the true y in Fig. 42. The performance is expected to degrade at small-y when calorimeter noise is included, but we are confident that this technique will allow to substantially extend the measurement range shown in Fig. 40.

The measurement of F_L requires running at different center-of-mass energies and comparing cross sections for a given x, Q^2 but different y, as is clear from the cross section formula

$$\frac{d^2\sigma}{dxdQ^2} = \frac{2\pi\alpha^2}{xQ^4}\left[Y_+ F_2(x,Q^2) - y^2 F_L\right]$$

where $Y_+ = 1 + (1-y)^2$, and xF_3 has been neglected. We have estimated the kinematic range where a 10 % or better measurement of $R = \frac{F_L}{F_2 - F_L}$ is possible using different proton beam energies ($920, 690, 460$ GeV). The results are shown in Fig. 43, along with two different set of predictions. As is clear from these plots, it will be possible to measure F_L with the required precision in the kinematic region of highest interest.

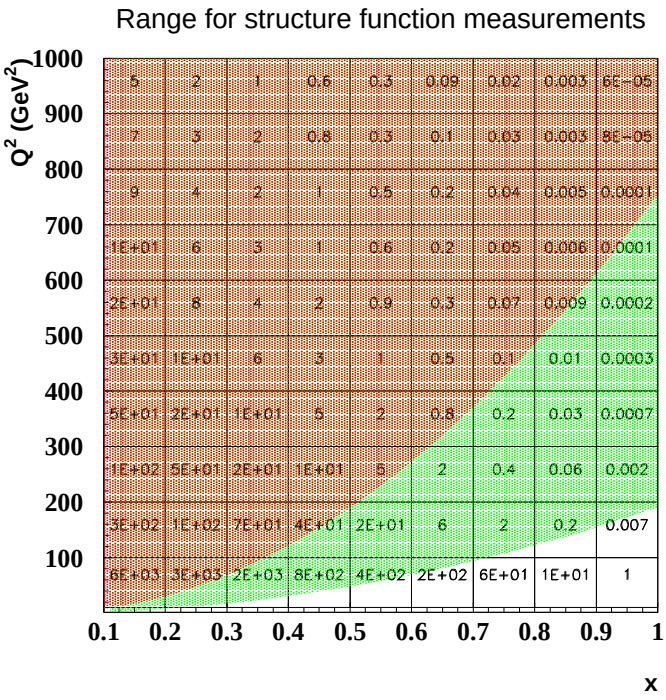

Figure 41: The cross sections at high-x and the expected region where the electron+jet method can be used. The red shaded area can be accessed with a proton beam energy of $E_P = 920$ GeV, while the green shaded area is accessible with $E_P = 460$ GeV. The electron energy is fixed at $E_e = 27.5$ GeV. The cross sections are estimated using the ALLM parametrization and are in units of pb.

The measurements of F_L will rely on a clean extraction of the low energy electron. The systematics associated with e/π separation have not yet been estimated, but will likely be the dominant error. It is for this reason that we have emphasized e/π separation at low energies.

3.3.2 Exclusive processes

The detector geometry will allow very good acceptance and event reconstruction at both high and low W for vector meson production and DVCS, thereby increasing the range of measurements which were possible with H1 and ZEUS. Figure 44 shows, for photoproduction of J/ψ, the J/ψ energy versus W, and the range typically covered by the tracking chambers of ZEUS and H1. A similar pattern will follow for other vector mesons. The W range covered for J/ψ photoproduction has been increased by both H1 and ZEUS by using calorimetric information to reconstruct the mass, but this is not possible for other vector mesons, or for DVCS. With the new detector, tracking and calorimetry will be available over nearly the full range of W, thereby allowing the identification of the process and event reconstruction over the full kinematic range. The long lever arm in W will allow the energy dependence of the cross sections to be measured with considerably higher precision. Another very important feature is that proton breakup events will be tagged with high efficiency with the proton remnant tagger described in section 3.2.5. The elastic cross sections can theferore be measured out to high $|t|$, with controllable backgrounds from proton dissociation events. The measurement of the t-distribution will be the biggest challenge. Resolutions on P_T of a few hundred MeV should be possible for the vector meson events using the tracking information, allowing t measurements out to $t = 1.5$ GeV^2. For the DVCS case, a combination of calorimetric information and kinematic constraints will be used to reconstruct the event kinematics.

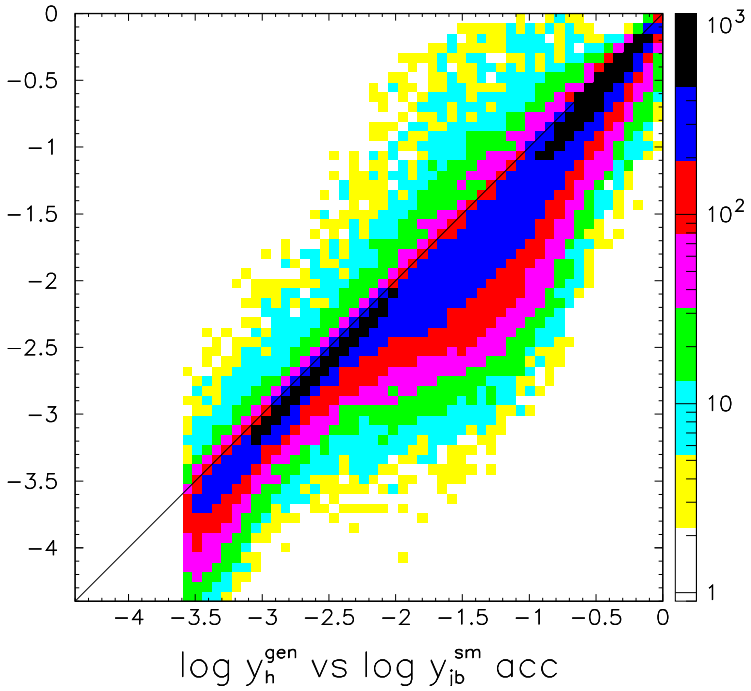

Figure 42: The generated *y* compared to the value reconstructed from the hadronic system.

3.3.3 Forward jets and particle production

One of the principal features of the detector is the possibility to track particles over a very wide rapidity range. The tracking acceptance in the proton direction is shown in Fig. 45, and extends to $\eta = 5$ for all momenta. This acceptance is to be contrasted with the maximum pseudo-rapidity coverage of H1 and ZEUS of $\eta \leq 1.75$. This vastly increased rapidity coverage will allow the measurement of particle production and particle correlations from the current jet region into the target fragmentation region, thereby allowing detailed studies of radiation patterns in QCD. The situation for forward jet production is also extremely advantageous, since the calorimetric coverage extends also to very high rapidities. Jet reconstruction should be possible out to $\eta = 5$, again allowing for much more sensitive tests of parton splitting processes. The acceptance of this detector is contrasted to that of the H1 and ZEUS detectors in Fig. 46. The visible cross section for forward jet production is also given in Fig. 46.

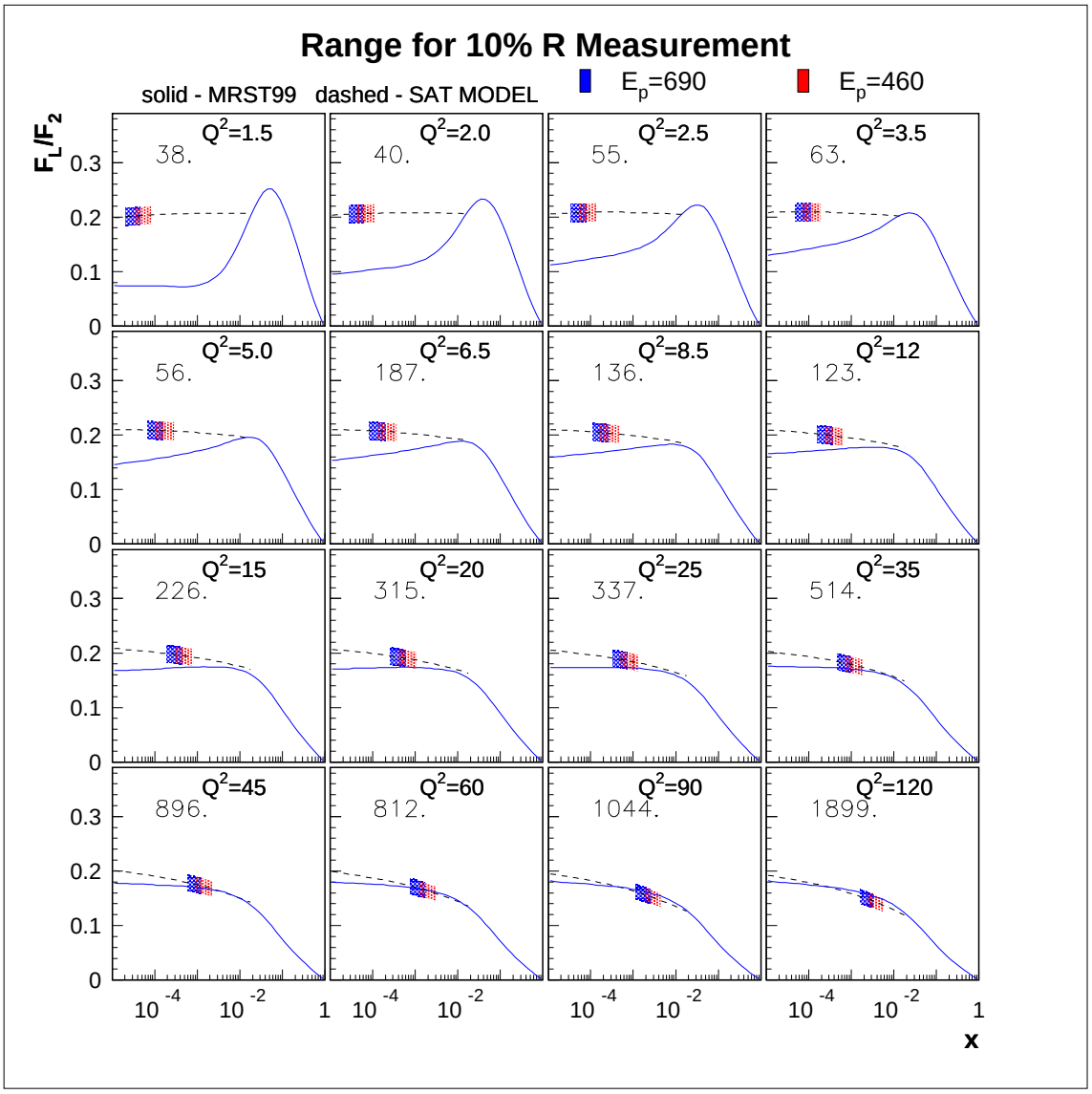

Figure 43: The x-range where we expect to make a 10 % or better measurement of F_L is shown in different Q^2 bins. The red shaded area uses the data from ($E_P = 920, E_P = 460$ GeV), while the blue shaded area uses the combination ($E_P = 920, E_P = 690$ GeV). The required luminosity is given in each bin in the upper left corner (in pb^{-1}). Note that bins will be combined at high Q^2 to make a reasonable measurement.

4 Summary, scope and time scale

Physics summary A new program of HERA running would yield valuable information on the high energy limit of strong interactions. The highlights of the program are seen as precision measurements of the structure functions F_2 and F_L, measurements of forward jet and particle production in small-x events in an extended rapidity range and measurements of exclusive processes, in particular at high t. These measurements should be performed for protons, deuterons, and at least one heavy nucleus. A new detector optimized for this physics program would greatly enhance the kinematic range covered today by H1 and ZEUS. Precision measurements of F_2 would be possible in a continuous way across the partons-to-hadrons transition region, where current data are sparse but very interesting. F_2 would also be measureable with good statistics up to $x \approx 1$ for $Q^2 > 200$ GeV^2, which to date is a completely unexplored region. F_L would be measured directly at HERA for the first time and with good precision in the region of greatest interest, $Q^2 \leq 10$ GeV^2, where we currently have large theoretical

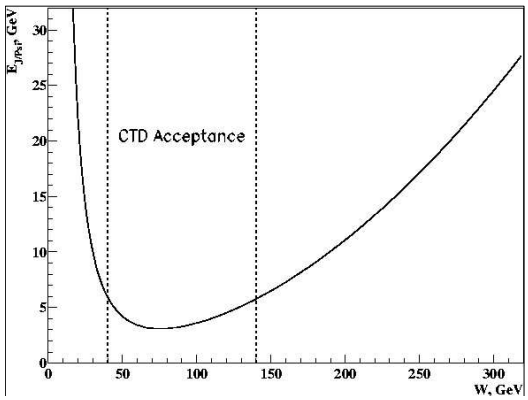

Figure 44: The J/ψ energy versus W, and the range covered by the central trackers of ZEUS and H1.

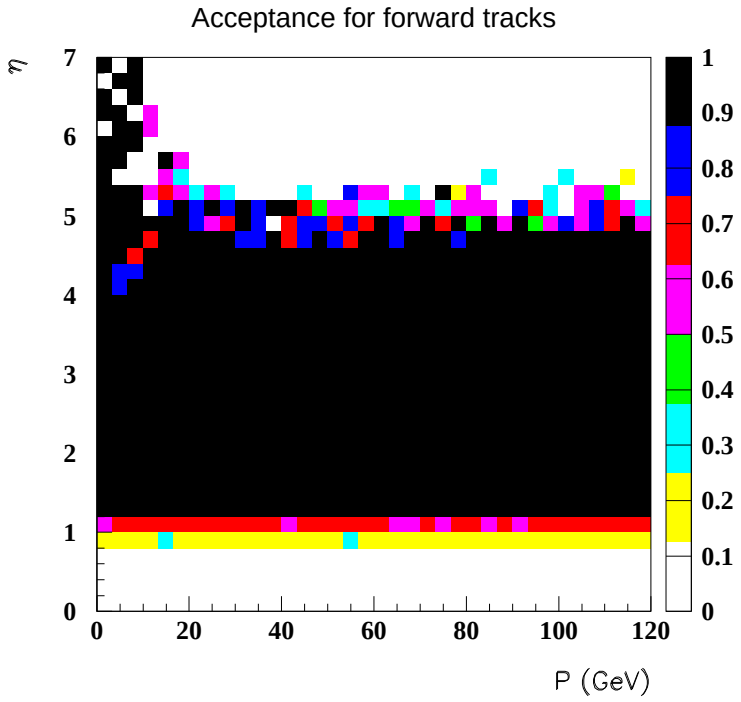

Figure 45: The acceptance of the tracking system in the proton direction. A track is considered accepted if it has crossed at least three tracking stations.

uncertainties. Exclusive vector meson production and DVCS could be studied across the full W range and up to $|t| \leq 1.5$ GeV^2, thereby allowing a much higher precision determination of the energy dependence of the cross sections, and a three-dimensional mapping of hadrons down to small impact parameters. The study of forward jet production and particle production over a wide range of pseudorapidities (up to $\eta = 6$, compared to $\eta = 2.7$ at H1, ZEUS) would allow stringent tests of our understanding of radiation processes in QCD, as well as show us where collective phenomena become important. Performing these measurements for the first time on deuterons would allow us to test the universality of parton distributions at small-x, as well as allow an extraction of individual parton densities at high-x. Scattering on a heavy nucleus such as Mercury would test the onset of saturation effects, with the possible discovery of the gluon condensate. These data would also be

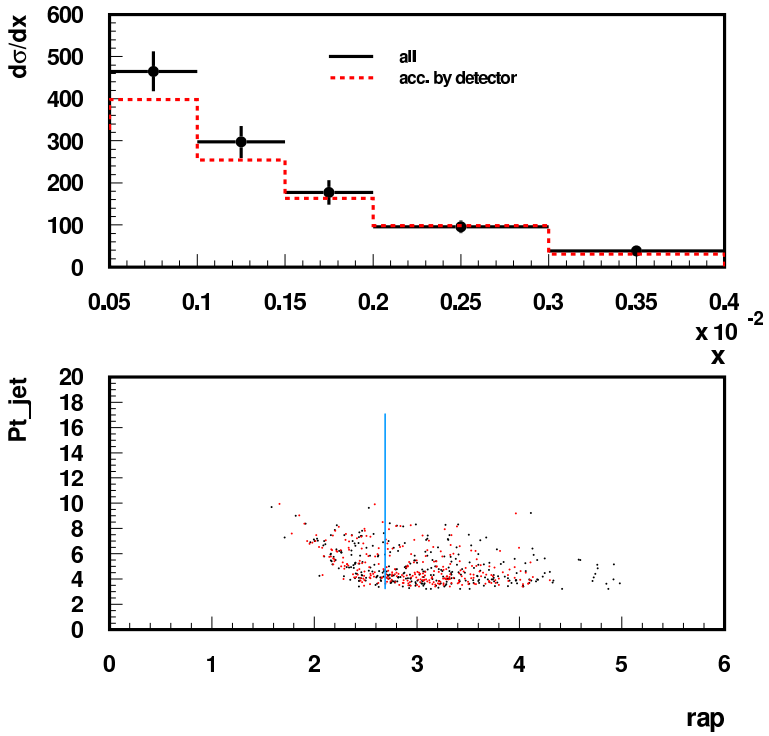

Figure 46: The comparison of generated and accepted cross section for events with a forward jet is shown in the top figure. The lower figure shows the acceptance for forward jets in the η and P_T plane. The range covered by H1 and ZEUS is to the left of the blue line.

invaluable for the interpretation of heavy ion scattering experiments. These measurements are critical for the further development of our understanding of strong interaction physics.

New detector summary The major subcomponents of the proposed detector are

- the precision tracking system;
- the 4π electromagnetic calorimeter;
- the forward hadronic calorimeter;
- the dipole magnet and beampipe.

In addition, we foresee the need for a photon calorimeter downstream in the electron direction, and several small detectors in the proton beam direction

- a proton remnant tagger at $z \approx 20$ m;
- a forward neutron calorimeter;
- a forward proton calorimeter.

Some of the detector elements could potentially come from existing experiments. The scale of the experiment is intermediate between a typical fixed target experiment and a typical collider experiment. A first, crude, estimate of the cost is 50 MEuro, approximately evenly divided between the tracking system, the electromagnetic calorimeter, and the beamline (including the dipole). This estimate assumes the hadron calorimeter would come from other sources.

We would aim to complete the design and construction of the detector within five years. A possible schedule would therefore be as follows:

2003 Prepare letter of intent and proposal;

2004 Detector design and R&D;

2005-7 Detector construction;

2008 Detector installation;

2009- Detector commissioning and operation.

The running schedule is flexible at this point. We however anticipate requiring data sets of roughly 50 pb^{-1} at each for three different proton energies for *eP* collisions. For nuclear targets, a few pb^{-1} is sufficient to study the universality of partons at small-*x* with deuterons, and early estimates indicate that a few 10 nb^{-1} are sufficient for a heavy target such as Mercury. It would be advantageous to be able to run HERA with different beam energies also for nuclei.

The small-*x* (or high energy) physics opened up by HERA should now be pursued with a new round of experiments. Many key measurements could not be carried out with H1 and ZEUS, as these detectors were designed for a different physics. Other important measurements require the addition of nuclei to be carried out. A dedicated experiment optimized for this physics would significantly enhance our understanding of QCD in its high energy limit, and possibly open the way to a complete revision of our ideas on the strong interactions.

HERA is the ideal place for the measurement program described in this expression of interest: it is an existing collider which has demonstrated the performance necessary for the measurements; and it is the high energy frontier for deeply inelastic scattering.

References

[1] A. D. Martin, R. G. Roberts, W. J. Stirling and R. S. Thorne, Eur. Phys. J. C **23** (2002) 73 [arXiv:hep-ph/0110215].

[2] S. Chekanov *et al.* [ZEUS Collaboration], Phys. Rev. D **67** (2003) 012007 [arXiv:hep-ex/0208023].

[3] C. Adloff et al., [H1 Collaboration], Eur. Phys. J. **C21** (2001) 33.

[4] B. Abbott *et al.* [D0 Collaboration], Phys. Rev. Lett. **86** (2001) 1707 [arXiv:hep-ex/0011036].

[5] T. Affolder *et al.* [CDF Collaboration], Phys. Rev. D **64** (2001) 032001 [Erratum-ibid. D **65** (2002) 039903] [arXiv:hep-ph/0102074].

[6] S. Catani, Z. Phys. C **70**, 263 (1996) [arXiv:hep-ph/9506357] Z. Phys. C **75**, 665 (1997) [arXiv:hep-ph/9609263].

[7] R. Thorne, "Measurements of $F_L(x,Q^2)$ at HERA-III", presentated at the HERA-III Workshop, "The New Frontier in Precision Lepton-Nucleon Physics", Muenich, December 2003.

[8] M. Gluck and E. Reya, Phys. Lett. B **83** (1979) 98;
R. S. Thorne and R. G. Roberts, Phys. Rev. D **57** (1998) 6871 [arXiv:hep-ph/9709442].

[9] E. Levin, Mini-rapporteur talk at EPS91, Geneva,DESY 91-110; Review talk at DIS94, Eilat, 1994, in the proceedings and Fermilab-conf-98/068-T.

[10] J. Bartels and C. Bontus, Phys. Rev. D **61**, 034009 (2000) [arXiv:hep-ph/9906308]; J. Bartels, K. Golec-Biernat and K. Peters, Eur. Phys. J. C **17**, 121 (2000) [arXiv:hep-ph/0003042].

[11] For a review see M. F. McDermott, arXiv:hep-ph/0008260, and references therein.

[12] K. Golec-Biernat and M. Wusthoff, Phys. Rev. D **59** (1999) 014017 [arXiv:hep-ph/9807513].

[13] H1 Collab., "A New Measurement of the Deep Inelastic Scattering Cross Section and of F_L at Low Q^2 and Bjorken-x at HERA ", H1prelim-01-041.

[14] E. L. Berger and S. J. Brodsky, Phys. Rev. Lett. **42** (1979) 940; Y. L. Dokshitzer, G. Marchesini and B. R. Webber, Nucl. Phys. B **469** (1996) 93 [arXiv:hep-ph/9512336]; E. Stein, M. Maul, L. Mankiewicz and A. Schafer, Nucl. Phys. B **536** (1998) 318 [arXiv:hep-ph/9803342].

[15] J. P. Ralston and B. Pire, Phys. Rev. **D66**, 111501 (2002), hep-ph/0110075.

[16] M. Diehl, Eur. Phys. J. **C25**, 223 (2002), hep-ph/0205208.

[17] M. Burkardt, Int. J. Mod. Phys. A **18**, 173 (2003), hep-ph/0207047.

[18] J. Bartels and H. Kowalski, Eur. Phys. J. C **19**, 693 (2001) hep-ph/0010345.

[19] D. Müller, D. Robaschik, B. Geyer, F. M. Dittes, and J. Hořejši, Fortschr. Phys. **42**, 101 (1994), hep-ph/9812448.

[20] X.-D. Ji, Phys. Rev. Lett. **78**, 610 (1997), hep-ph/9603249.

[21] A. V. Radyushkin, Phys. Rev. **D56**, 5524 (1997), hep-ph/9704207.

[22] J. C. Collins, L. Frankfurt, and M. Strikman, Phys. Rev. **D56**, 2982 (1997), hep-ph/9611433.

[23] J. Blümlein, B. Geyer and D. Robaschik, Nucl. Phys. B **560**, 283 (1999), hep-ph/9903520.

[24] S. Munier, A. M. Stasto, and A. H. Mueller, Nucl. Phys. **B603**, 427 (2001), hep-ph/0102291.

[25] A. Freund, M. McDermott and M. Strikman, Phys. Rev. D **67** (2003) 036001 [arXiv:hep-ph/0208160].

[26] M. Ciafaloni, *Nucl. Phys.* **B 296** (1988) 49.

[27] S. Catani, F. Fiorani, G. Marchesini, *Phys. Lett.* **B 234** (1990) 339.

[28] S. Catani, F. Fiorani, G. Marchesini, *Nucl. Phys.* **B 336** (1990) 18.

[29] G. Marchesini, *Nucl. Phys.* **B 445** (1995) 49.

[30] B. Andersson, G. Gustafson, J. Samuelsson, *Nucl. Phys.* **B 467** (1996) 443.

[31] B. Andersson, G. Gustafson, H. Kharraziha, J. Samuelsson, *Z. Phys.* **C 71** (1996) 613.

[32] G. Gustafson, H. Kharraziha, L. Lönnblad, The LCD Event Generator, in *Proc. of the Workshop on Future Physics at HERA*, edited by A. De Roeck, G. Ingelman, R. Klanner (1996), p. 620.

[33] H. Kharraziha, L. Lönnblad, *JHEP* **03** (1998) 006.

[34] G. 't Hooft, *Nucl. Phys.* **B190** (1981) 455.

[35] J. D. Bjorken, K. L. Kowalski, C. C. Taylor, (1993) .

[36] B. Andersson, G. Gustafson, J. Samuelsson, *Z. Phys.* **C64** (1994) 653.

[37] T. Sjostrand et al., *Comput. Phys. Commun.* **135** (2001) 238, hep-ph/0010017.

[38] G. Marchesini et al., *Comp. Phys. Comm.* **76** (1992) 465, hep-ph/9912396.

[39] A. Mueller, *Nucl. Phys.* **B** *(Proc. Suppl)* **18C** (1990) 125.

[40] A. Mueller, *J. Phys.* **G 17** (1991) 1443.

[41] H1 Collaboration, C. Adloff et al., *Nucl. Phys.* **B 538** (1999) 3.

[42] ZEUS Collaboration; J. Breitweg et al., *Eur. Phys. J.* **C 6** (1999) 239.

[43] H. Jung, G. Salam, *Eur. Phys. J.* **C 19** (2001) 351, hep-ph/0012143.

[44] L. Lönnblad, *Comp. Phys. Comm.* **71** (1992) 15.

[45] N. B. et al., A comparison of deep-inelastic Monte Carlo event generators, in *Proceedings of the Workshop on Monte Carlo generators for HERA physics*, edited by A. Doyle, G. Grindhammer, G. Ingelman, H. Jung (DESY, Hamburg, 1999), p. 10.

[46] G. Ingelman, A. Edin, J. Rathsman, *Comp. Phys. Comm.* **101** (1997) 108.

[47] H. Jung, *Comp. Phys. Comm.* **143** (2002) 100, hep-ph/0109102, DESY 01-114, `http://www.quark.lu.se/ hannes/`

[48] R.K. Ellis and P. Nason, Nucl. Phys. B 312 (1989) 551;
S. Frixione et al., Nucl. Phys. B412 (1994) 225;
M. Mangano et al., Nucl. Phys. B373 (1992) 295.

[49] M. Cacciari et al., Z. Phys. C69 (1996) 459; Phys. Rev. D55 (1997) 2736;
M. Cacciari and M. Greco, Phys. Rev. D55 (1997) 7134;
B.A. Kniehl et al., Z. Phys. C76 (1997) 689;
J.Binnewies et al., Z. Phys. C76 (1997) 677; Phys. Rev. D58 (1998) 014014.

[50] M. Cacciari, S. Frixione and P. Nason, JHEP 0103, 006 (2001);
S. Frixione and P. Nason, JHEP 0203, 053 (2002).

[51] P. Nason, Heavy Flavour Production, hep-ph/0207362, invited talk in Vietri Heavy Quark and Leptons conference, June 2002, Salerno, Italy.

[52] ZEUS Collaboration, paper 786 submitted to the XXXI Int. Conf. on High Energy Physics, July 2002, Amsterdam, The Netherlands.

[53] ZEUS Collaboration, paper 783 submitted to the XXXI Int. Conf. on High Energy Physics, July 2002, Amsterdam, The Netherlands.

[54] S. Frixione, P. Nason and G. Ridolfi, Nucl. Phys. B 454 (1995), 3.

[55] EMC, J.J. Aubert et al., Phys. Lett. B123 (1983) 275.

[56] SLAC, J. Aubert et al., Phys. Lett. B123 (1983) 275;
NMC, P. Amaudruz et al. (NMC), Nucl. Phys. B441 (1995) 3;
NMC, M. Arneodo et al. (NMC), Nucl. Phys. B441 (1995) 12.

[57] NMC, M. Arneodo et al., Nucl. Phys. B481 (1996) 23.

[58] T. Gousset, H.J. Pirner, Phys. Lett. B375 (1996) 349.

[59] L. Frankfurt, M. Strikman, Eur. Phys. J. A5 (1999) 293.

[60] K.J. Eskola et al., Phys. Lett. B532 (2002) 222.

[61] S.J. Brodsky al., hep-ph/0104291.

[62] K. Golec-Biernat, Acta Phys. Polon. B33 (2002) 2771.

[63] A. Freund et al., Acta Phys. Polon. B33 (2002) 3057.

[64] B.B. Back et al., Phobos Collaboration, Phys. Rev. C65, (2002) 061901 nucl-ex/0201005

[65] M.W. Krasny contribution to “Future Physics at HERA”, Proc. Workshop, DESY 1996/97, Ed.s G. Ingelman, A. De Roeck and R. Klanner.

[66] J. Andruszków et al., Acta Phys. Pol. B32 (2001) 2025.

[67] L. Suszycki, Luminosity Monitoring, Photon Tagging and QED Tests, in Proc. of the HERA Workshop, vol 2, p.503, Hamburg 1987.

[68] V. Andreev et al., NIM A494 (2002) 45.

[69] P. Gorodetzky et al., NIM A361 (1995) 161;
N. Akchurin et al., NIM A399 (1997) 202.

[70] G. Levman contribution to “Future Physics at HERA”, Proc. Workshop, DESY 1996/97, Ed.s G. Ingelman, A. De Roeck and R. Klanner.

[71] S. Bhadra et al., Nucl. Instr. and Meth. A 394 (1997) 121; ZEUS Collaboration, Paper 440, submitted to XXX International Conference on High Energy Physics, Osaka, 2000.

[72] M. W. Krasny, Determination of the Longitudinal Structure Function at HERA from Radiative Events, in Proc. of the Workshop on the Physics at HERA, W. Buchmüller and G. Ingelmann, eds.) vol. 1, p 171, Hamburg, 1991.

[73] A. Bornheim, Ph D Thesis, BONN-IR-99-17, Bonnn University, Oct. 1999.
J. P. Scott, Ph D Thesis, Bristol University, Oct. 2000.

[74] P.Nevski *An interactive tool for GEANT* ATLAS software note 002, 1994

[75] H. Abramowicz and A. Levy, DESY Report 97-251 (1997).